VARIOUS METHODS IN SHAPE ANALYSIS AND IMAGE SEGMENTATION AND REGISTRATION

By

JUNG-HA AN

A DISSERTATION PRESENTED TO THE GRADUATE SCHOOL
OF THE UNIVERSITY OF FLORIDA IN PARTIAL FULFILLMENT
OF THE REQUIREMENTS FOR THE DEGREE OF
DOCTOR OF PHILOSOPHY

UNIVERSITY OF FLORIDA

2005

Copyright 2005

by

Jung-Ha An

In dedication to Dok-Me An.

TABLE OF CONTENTS

page

LIST OF TABLES vi

LIST OF FIGURES vii

ABSTRACT x

CHAPTER

1 INTRODUCTION 1

2 AN EDGE-BASED ACTIVE CONTOUR MODEL WITH PRIOR SHAPE AND INTENSITY PROFILE FOR SIMULTANEOUS SEGMENTATION AND NON-RIGID REGISTRATION 9

2.1 Introduction 9
2.2 Background Review; Active Contours 11
2.3 Generating Prior Shape and Intensity information 13
2.3.1 Area Difference Distance Measurement 13
2.3.2 Generating Prior Mean Shape and Clustering 14
2.4 Description of the Proposed Model 15
2.5 Level Set Formulation of the Proposed Model 17
2.5.1 Level Set Formulation 17
2.5.2 Euler-Lagrange Equations: 18
2.6 Numerical Methods 19
2.7 Experimental Results 21
2.8 Generating Prior Mean Shape and Clustering 27
2.8.1 Generating Mean Shape with Orthogonal Procrustes Measurement 29
2.8.1.1 Orthogonal Procrustes Method. 29
2.8.1.2 Description of the Suggested Model 30
2.8.1.3 Experimental Results 31
2.8.2 Generating Mean Shape and Clustering using Self-Organizing Map 33
2.8.2.1 Description of the Self-Organizing Map(SOM) . . . 33
2.8.2.2 Self-Organizing Map with Procrustes Methods . . . 34
2.8.2.3 Self-Organizing Map Combined with Principal Component Analysis 35
2.8.2.4 Experimental Results 35

3 A REGION-BASED MODEL FOR IMAGE SEGMENTATION AND REGISTRATION 40

3.1 Image Segmentation Using a Modified Mumford-Shah Technique . . 40
3.1.1 Introduction 40
3.1.2 Description of a Modified Mumford-Shah Model 43
3.1.2.1 Euler-Lagrange Equations of the Model 44
3.1.3 Numerical Methods 44
3.1.4 Experimental Results 45
3.2 Region Based Segmentation with Shape Prior 48
3.2.1 Introduction 48
3.2.2 Description of the Proposed Model 50
3.2.2.1 Euler-Lagrange Eqnations of the Proposed Model . 51
3.2.3 Numerical Methods 52
3.2.4 Experimental Resnlts 53
3.3 Simultaneous Segmentation and Registration using a Modified Mumford-Shah Model 55
3.3.1 Introduction 55
3.3.2 Description of the Proposed Model 57
3.3.2.1 Euler-Lagrange Equations of the Proposed Model . 58
3.3.3 Numerical Methods 60
3.3.4 Experimental Results 61

4 CONCLUSIONS AND FUTURE DIRECTION 64

REFERENCES 68

BIOGRAPHICAL SKETCH 75

LIST OF TABLES

Table		page
2-1	Distance Measurements of the Result of the Model from Expert's Borders from Figure 2-2 to Figure 2-3	25
2-2	Distance Measurements of the Result of the Model with Non-Rigid Term from Expert's Borders from Figure 2-4 to Figure 2-7	26
2-3	Distance Measurements of the Result of the Model with Rigid Term Only from Expert's Borders from Figure 2-4 to Figure 2-7	26
2-4	The Parameters Used for Figure 2-4 through Figure 2-7 with Non-Rigid Term	27
2-5	The Parameters Used for Figure 2-4 through Figure 2-7 with Rigid Term Only	27
2-6	Distance Measurements of the Result of the Models from Figure 2-8, n=85	32
2-7	Distance Measurements of the Result of the Models from Figure 2-9 to Figure 2-11. M_d Represents Mean Distance. STD_d Represents Standard Deviation. T_d Represents Tanimoto Distance with n=85	38
2-8	Distance Measurements of the Result of the Models from Figure 2-12. M_d Represents Mean Distance. STD_d Represents Standard Deviation. T_d Represents Tanimoto Distance	38
2-9	Distance Measurements of the Result of the Models from Figure 2-13. M_d Represents Mean Distance. STD_d Represents Standard Deviation. T_d Represents Tanimoto Distance	39

LIST OF FIGURES

Figure page

2–1 (a)A Prior Intensity I^* (b)A Prior Shape C^* as a Solid Line 16

2–2 Subject 2 : Solid Line by Our Model Result and Dotted Line by Expert (a)A Initial Contour. (b) Model with $\lambda_1 = 0$. (c) Model with $\lambda_2 = 0$ . . . 24

2–3 Subject 2 : Solid Line by Our Model Result and Dotted Line by Expert (a) Model with $\lambda_3 = 0$. (b) Model with $\lambda_4 = 0$ 24

2–4 Subject 1 : Solid Line by Our Model Result and Dotted Line by Expert (a)An Initial Contour (b) Model with Non-Rigid Term, (c) Model with Rigid Term Only 25

2–5 Subject 2 : Solid Line by Our Model Result and Dotted Line by Expert (a)An Initial Contour (b) Model with Non-Rigid Term, (c) Model with Rigid Term Only 25

2–6 Subject 3 : Solid Line by Our Model Result and Dotted Line by Expert (a)An Initial Contour (b) Model with Non-Rigid Term, (c) Model with Rigid Term Only 25

2–7 Subject 4 : Solid Line by Our Model Result and Dotted Line by Expert (a)An Initial Contour (b) Model with Non-Rigid Term, (c) Model with Rigid Term Only 26

2–8 Left : A Initial Contour. Right : The Results are from the Shape Related Energy Function with the Mean Shape as a Dotted Line with 85 human-heart end-diastolic epicardial borders 32

2–9 Two Chamber ED EPI Normal 85 Patients Heart Contours with 5000 Iterations using SOM + Area Difference Method. The Dotted Line Represents the Average of the Cluster with n=85 37

2–10 Two Chamber ED EPI Normal 85 Patients Heart Contours with 5000 Iterations using SOM + orthogonal Procrustes method. The Dotted Line Represents the Average of the Cluster with n=85 37

2–11 Two Chamber ED EPI normal 85 Patients Heart Contours with 5000 Iterations using SOM + PCA. The Dotted Line Represents the Average of the Cluster with n=85 38

2–12 Two Chamber ED EPI Normal 85 Patients Heart Contours with 5000 Iterations into 3 Groups using SOM+Orthogonal Procrustes Measurement. The Dotted Line Represents the Average of the Cluster with n=85. Left : 30 contours, Middle : 28 contours, Right : 27 contours 38

2–13 Two Chamber ED EPI Normal 85 Patients Heart Contours with 5000 Iterations using SOM + PCA. The Dotted Line represents the Average of the Cluster with n=85. Left : 30 contours. Middle : 28 contours. Right : 27 contours 39

3–1 Left : A Novel Image, Middle : $\theta(\bar{x}), \bar{x} \in \Omega$, Right : Segmented Image by $H(\phi(\bar{x})), \bar{x} \in \Omega$ 46

3–2 Left : A Novel Image, Right : The Boundary of the Segmented Image . . 46

3–3 Left : c_1 values, Right : c_2 values in each iteration from Figure 3-1 46

3–4 Left : A Novel Image, Middle : $\theta(\bar{x}), \bar{x} \in \Omega$, Right : Segmented Image by $H(\phi(\bar{x})), \bar{x} \in \Omega$ 47

3–5 Left : A Novel Image, Right : The Boundary of the Segmented Image . . 47

3–6 Left : c_1 values, Right : c_2 values in each iteration from Figure 3-4 48

3–7 Left : A Novel Image, Middle : $\theta(\bar{x}), \bar{x} \in \Omega$, Right : Segmented Image by $H(\phi(\bar{x})), \bar{x} \in \Omega$ 48

3–8 Left : A Novel Image, Right : The Boundary of the Segmented Image . . 49

3–9 Left : c_1 values, Right : c_2 values in each iteration from Figure 3-7 49

3–10 Left : Simulated MRI image BI. Right : S 54

3–11 Left : A Novel Image I. Middle : Segmented Image, Right : The Boundary of the Segmented Image 54

3–12 Left : Simulated MRI image BI. Right : S 54

3–13 Left : A Novel Image I. Middle : Segmented Image, Right : The Boundary of the Segmented Image 55

3–14 Left : A Novel Image I_1, Middle : A Novel Image I_2, Right : Segmented Image of I_1 62

3–15 Left : The Boundary of the Segmented Image I_1, Middle : Segmented Image of I_2, Right : The Boundary of the Segmented Image of I_2 62

3–16 Left : A Novel Image I_1, Middle : A Novel Image I_2, Right : Segmented Image of I_1 63

3–17 Left : The Boundary of the Segmented Image of I_1, Middle : Segmented Image of I_2, Right : The Boundary of the Segmented Image of I_2 63

Abstract of Dissertation Presented to the Graduate School
of the University of Florida in Partial Fulfillment of the
Requirements for the Degree of Doctor of Philosophy

VARIOUS METHODS IN SHAPE ANALYSIS AND
IMAGE SEGMENTATION AND REGISTRATION

By

Jung-Ha An

December 2005

Chair: Yunmei Chen
Major Department: Mathematics

Image segmentation and registration are vital to image processing, image analysis, and computer vision. In the last decade, research into these areas has developed at a rapid pace by using various mathematical methods. In this dissertation, variational partial differential equations are proposed to solve image segmentation and registration problems.

A new variational partial differential equation based level set method for simultaneous image segmentation and non-rigid registration is presented. This technique incorporates both prior shape and intensity information. Since global rigid registration has limited applicability when non-rigid shapes are considered, a transformation is created which is the sum of a global rigid function and a local non-rigid deformation. This model is tested against two-chamber end-systolic endocardial ultrasound images of thirteen human patients. The experimental results provide preliminary evidence of the effectiveness of the model in detecting the boundaries of the incompletely resolved objects which were plagued by noise, dropout, and artifact. Develop algorithms for generating the mean shape has a significant role in image segmentation, since the mean shape can be used as a prior

shape to acquire better segmentation results. As alternate ways, several statistical algorithms including a shape related energy function, Self-Organizing map with Procrustes methods, and Self-Organizing map with a principal component analysis to generate mean shape and clustering are also presented.

Region based image segmentation and registration models which contains three interrelated sections: image segmentation using a modified Mumford-Shah technique, region based segmentation using a prior shape, and simultaneous segmentation and registration using Mumford-Shah model are also proposed. The first goal is to develop an image segmentation technique using a modified Mumford-Shah model. A variational region intensity based image segmentation model is presented. The boundary of the given image is extracted using a modified Mumford-Shah segmentation technique. Even though the two phase case is performed for image segmentation during the numerical experiments, the suggested model can be applied to more general cases. Another goal is to develop a region based image segmentation technique using prior shape information. The prior shape information is extracted by using a modified Mumford-Shah segmentation technique. The prior shape knowledge supports the segmentation process for a novel image. Finally, a region based model for simultaneous image segmentation and registration is also presented. The purpose of the model is to segment and register given images simultaneously utilizing a modified Mumford-Shah technique and region intensity values. The segmentation is obtained by minimizing a modified Mumford-Shah model. A global rigid registration is assisted by the segmentation information and region intensity values. A segmentation and registration process is obtained simultaneously in this model. In addition, the model can also be applied to the case of non-rigid registration. The numerical experiments of the proposed models are tested against synthetic data and simulated human brain MRI images.

The experimental results provide preliminary evidence of the effectiveness of the proposed models.

CHAPTER 1
INTRODUCTION

Developing algorithms for solving image segmentation and registration problems have become an important and active area of research. These methods have been applied to a wide range of problems in computer vision, pattern recognition, object recognition, image processing, and image analysis. There have been a multitude of different approaches for separately solving image segmentation and registration problems. One goal of this research is to develop a method which solves segmentation and registration problems simultaneously.

Segmentation techniques have been developed to capture the boundary of an object by several different approaches; edge-based methods using active contour models developed by Caselles, Kimmel, Sapiro, Kass, Olver, Sethian, Vemuri, Yezzi, et al. [7, 8, 33, 38, 47, 86], which rely on the information of the edges, namely high magnitude of the image gradient; region-based methods proposed by Chan, Vese, Cremers, Tsai, Mumford, Shah, Yezzi, Zhu, et al. [9, 10, 19, 22, 57, 75, 87, 93] that depend on the region statistics or homogeneity; or a combination of the two presented by Paragios and Deriche [60, 61, 62] using Geodesic Active Region models. However, these methods may not be able to accommodate all types of imaging difficulties that occur in images, including significant signal loss, noise, and non-uniformity of regional intensities. Therefore, prior information is necessary to make the resulting segmentation more accurate. The prior shape and intensity information has been incorporated into the geodesic active contour model presented by Chen, Leventon, Faugeras, et al. [12, 13, 14, 15, 41, 42]. The details are available in Chen, Huang, et al. [13]. Recently, the prior shape and intensity information has been also incorporated into deformable models proposed by

Metaxas, Huang, et al. [31, 32]. A class of deformable models called MetaMorphs which possess both shape and interior texture statistics integrate boundary and region information coherently in a common variational framework [32]. The MetaMorphs models [32] are extended into a unified shape and intensity space by implicitly representing shapes as images in the space of distance transforms. A novel stochastic chord based matching algorithms align global transformation considering both shape and gray-level intensity information. The complementary local registration is performed by deforming a Free Form Deformation control lattice to maximize mutual information between both shape and intensity images [31].

Image registration is the process of overlaying two or more images of the same scene or similar scene taken at different times, and/or by different sensors. Area based methods or feature based methods have been developed to match given images. For the details of the image registration techniques, refer to [92] presented by Zitova and Flusser. Multi-modal registration combined with mutual information (MI) proposed by Hata, Maes, Viola, Wells, et al. [27, 46, 80, 83] generated a new class of rigid/affine registration algorithms. Nonlinear registration is the set of techniques that allow the alignment of data sets that are mismatched in a nonlinear or nonuniform manner. Dense correspondences between pairs and groups of images were generated using non-rigid algorithms presented by Bro-Nielsen, Chefd'Hotel, Faugeras, Gee, Marsland, Rueckert, et al. [5, 11, 25, 51, 69]. Several approaches have been made in establishing the application of mutual information for non-rigid registration proposed by Gaens, Hermosillo, Hellier, Likar, Meyer, Rueckert, et al. [24, 28, 29, 44, 54, 68]. Further improvements of these methods have been done by either the inclusion of some prior information on the joint intensity distribution (e.g. Likar and Permus [44]) or the use of higher order definitions of mutual information which incorporates spatial information (e.g. Rueckert, Clarkson, et

al. [68]). Instead of intensity information, a feature based model combines region matching and segmentation with free boundary conditions in Richard and Cohen [67]. However, the model in Richard and Cohen [67] can be applied only in a single region of interest.

However, segmentation or registration technique alone, dependence of segmentation on registration methods, or dependence of registration on segmentation methods does not solve the image segmentation and registration problems completely. Recently, joint segmentation and registration methods have been developed through the use of active contours proposed by Chen, Yezzi, Young, et al. [13, 15, 88, 89, 90]. An explicit combination of registration with segmentation has been developed in a variational framework through active contours by Yezzi, Zollei, and Kapur [88, 89]. Moelich and Chan[56] extend the algorithms of Yezzi, Zollei, and Kapur [88] to joint segmentation and of an object in two images, and the prior knowledge is implicitly incorporated through the simultaneous evolution of the registration maps and the active contour in the variational framework. In Chen, Tagare, et al. [15], the shape model was created by averaging the aligned training samples. Better maps were gathered by matching the evolving interface to the shape prior. The geometric active contour was minimized and the shape disparity energy function between the active contour and prior shape was measured by a distance function. This algorithm was extended in Chen, Guo, et al. [14] by incorporating the information on the location of a few key points gathered from standardized results. Instead of using a few key points by Chen, Guo, et al. [14], an intensity profiling term was added to match the intensity of the interface to the prior intensity cross prior shape and the active contour in Chen, Huang, et al. [13]. The mutual information intensity profiling and the determination of the parameter which balances the influence from image information and shape prior were developed in Chen, Huang, et al. [12] similar to Chen, Huang, Wilson, et al. [13].

The morphing active contours algorithm is combined with the joint segmentation and registration to deal with the complexity of segmenting real images with an application to CT scans for radiotherapy treatment planning by Young and Levy [90].

The purpose of Chapter 2 is to develop an algorithm to solve simultaneous image segmentation and registration problem. An edge-based active contour model using prior shape and intensity profile is suggested for solving simultaneous segmentation and registration problem in Chapter 2. In Chapter 2, a new variational PDE based level set method for simultaneous image segmentation and registration is presented with an application to two-chamber human-heart end-systolic endocardial ultrasound images. The purpose of the model is to segment the endocardial borders of the given images using prior shape and intensity profile. Prior shape and prior intensity of thirteen human-heart two-chamber epicardial ultrasound images were generated by the method in Chen, Feng, et al. [12]. The segmentation is obtained by finding a non-rigid registration to the prior shape. The model performs a simultaneous segmentation and registration in a way similar to Chen, Yezzi, et al. [13, 15, 88] through active contours. But the model differs from Chen, Yezzi, et al. [13, 15, 88] by using a shape prior as an initial contour. Since the shape prior is used as an initial contour, the level set form of the model is fixed which does not require the re-initialization process during the numerical calculation. The model in this chapter is similar to Chen, Leventon, et al. [12, 13, 41] , because it uses both prior shape and prior intensity information to produce the segmentation. The segmentation in this model is obtained by a non-rigid deformation from the prior shape. This model follows the idea from Huang, Metaxas, Paragios, Yezzi, et al. [31, 32, 63, 64, 71] for matching nonequivalent shapes by the combination of a global rigid transformation and a local non-rigid deformation. However, the

model differs from Paragios, Rousson, and Ramesh [63, 64] by having an intensity matching term in the energy function which provides the difference of the intensity variation across the prior shape and the shape of interest. Minimizing the difference of the gradients of the intensity between a smoothed prior image and a smoothed given image is more accurate than minimizing the gradient term in the given image, due to the loss of the information of the gradient near the edge of the desired object. Generating the mean shape has an important application to image segmentation, since it can be used as a prior shape to overcome all types of imaging difficulties. Chen, leventon, Paragios, Yezzi, Duncan, et al. [12, 13, 14, 15, 41, 42, 63, 64, 71, 85] showed that prior mean shape can play an important role to acquire better segmentation results. Several statistical methods for generating the mean shape and clustering are also presented as alternate techniques in Chapter 2. To create the mean shape, the shape related energy function is minimized with an orthogonal Procrustes measurement. The other model is introduced to generate the mean shape and clustering simultaneously using a Self-Organizing map combined with Procrustes methods. To measure the similarity between two contours, an area difference distance measurement proposed by Chen, Wilson, and Feng [16] and orthogonal Procrustes measurement [73] are used. In addition, a Self-Organizing map combined with a Principal Component Analysis model is also introduced to generate a better mean shape. These algorithms are applied to human heart epicardial cardiac borders trace by an expert on two-chamber end-systolic echo-cardiographic images. For verifying these results, mean distance, standard deviation, and Tanimoto distance measurement [40] are used to compare the results.

Chapter 2 is organized as follows: active contours are reviewed briefly in section 2.2. Generating prior shape and intensity information are explained in section 2.3. In section 2.4, the model is proposed for a simultaneous segmentation

and non-rigid registration and the level set form of the proposed model is described in section 2.5. In section 2.6, numerical methods pertaining to the model are explained. Experimental results of the model which were applied to human-heart two-chamber end-systolic ultrasound images are also shown in section 2.7. Several statistical methods with an application to human heart cardiac borders for generating the mean shape and clustering are presented in section 2.8.

The goal of Chapter 3 is to formulate various region based algorithms for solving image segmentation and registration problems. Several region-based algorithms for image segmentation and registration are proposed in Chapter 3, which contains three interrelated sections: image segmentation using a modified Mumford-Shah technique, region based image segmentation with prior shape, and a modified Mumford-Shah model based simultaneous segmentation and registration.

Mumford and Shah introduced the most celebrated region based image segmentation model in 1989 [57]. The measurement of an edge length term in the Mumford-Shah model is approximated by a quadratic integral of an edge signature function proposed by Ambrosio and Tortorelli in 1990 [1]. Chan and Vese proposed a piecewise constant Mumford-Shah model in [9, 10] Developments of variational level set implementation techniques based Mumford-Shah model are followed by Esedoglu, Gibou, Likar, et al. [22, 26, 43]. The segmentation is represented by characteristic functions using phase fields in Esedoglu, Likar, et al. [22, 43]. The details of phase field theory can be found in Baldo, Modica, Shen, Zhou, et al. [3, 55, 70, 82].

Recently, a soft Mumford-Shah segmentation is introduced in Shen [70]. The model in this section is motivated by Esedoglu, Shen, et al. [22, 70, 77].

In section 3.1, a region based variational partial differential equation model for an image segmentation is presented with an application to synthetic image and simulated human brain MRI images. The purpose of the model is to segment

borders of the given images. The segmentation is obtained by using a modified Mumford-Shah segmentation technique. In section 3.1.2, a modified Mumford-Shah model is proposed. The Euler-Lagrange equations of the suggested model are presented in this section as well. In section 3.1.3, numerical methods pertaining the proposed model are explained. The model is applied to synthetic data and simulated human brain MRI images are shown in section 3.1.4.

In section 3.2, a new variational image segmentation model based on the region intensity information utilizing shape knowledge is suggested. The goal of the model is to segment a given novel image using prior shape information. The prior shape knowledge is obtained by using modified Mumford-Shah segmentation technique in section 3.1. The prior shape knowledge is assisting the image segmentation process to a given novel image. In section 3.2.2, the model for generating prior shape information using a modified Mumford-Shah segmentation technique is described. In section 3.2.3, the proposed model is introduced. The Euler-Lagrange equations of the suggested model are presented in this section as well. The model is applied to synthetic data and simulated human brain MRI images are shown in section 3.2.4.

In section 3.3, a modified Mumford-Shah model based simultaneous segmentation and registration technique is presented. The purpose of the model is to segment and register given images simultaneously utilizing modified Mumford-Shah technique and region intensity values. The model performs a simultaneous segmentation and registration in a similar way from Yezzi, Zollei, and Kapur [88, 89]. But the model differs from Yezzi, Zollei, and Kapur [88, 89] by using a region intensity and modified Mumford-Shah segmentation technique. In section 3.3.2, the model is proposed for a simultaneous segmentation and registration and the Euler-Lagrange equations of the proposed model are described. In section 3.3.3, numerical methods pertaining to the model are explained. The model is applied to synthetic data and

simulated human brain MRI images are shown in section 3.3.4. Finally conclusions and future work are stated in Chapter 4.

CHAPTER 2
AN EDGE-BASED ACTIVE CONTOUR MODEL WITH PRIOR SHAPE AND INTENSITY PROFILE FOR SIMULTANEOUS SEGMENTATION AND NON-RIGID REGISTRATION

2.1 Introduction

The goal of image segmentation is to capture the boundary of an object. Using the information of the edges, namely high magnitude of the image gradient, edge-based methods have been developed using active contour models proposed by Caselles, Kimmel, Sapiro, Kass, Olver, Sethian, Vemuri, Yezzi, et al. [7, 8, 33, 38, 47, 48, 50, 53, 86]. To accommodate all types of imaging difficulties that occur in cardiac ultrasound images including significant signal loss, noise, and non-uniformity of regional intensities, the prior shape and intensity information has been incorporated into the geodesic active contour model presented by Chen, Leventon, Faugeras, et al. [12, 13, 14, 15, 41, 42]. Recently, the prior shape and intensity information has been also incorporated into deformable models proposed by Metaxas, Huang, et al. [31, 32].

Image analysis has been developed rapidly with applications to medical imaging, target tracking, and computer vision. Especially in medical imaging and target tracking, image registration play a significant role. Area based methods or feature based methods have been developed for image registration. Hata, Maes, Viola, Wells, et al. [27, 46, 80, 83] proposed multi-modal registration combined with mutual information (MI). This brought a new class of rigid/affine registration algorithms. Nonlinear registration is the set of techniques that allow the alignment of data sets that are mismatched in a nonlinear or nonuniform manner. Several approaches have been made in establishing the application of mutual information

for non-rigid registration presented by Gaens, Hermosillo, Hellier, Likar, Meyer, Rueckert, et al. [24, 28, 29, 44, 54, 68]. For the details of the image registration techniques, please refer to [92] presented by Zitova and Flusser.

Recently, joint segmentation and registration methods have been developed to get better image segmentation and registration results through active contours proposed by Chen, Yezzi, Young, et al. [13, 15, 88, 89, 90].

In Chapter 2, a new variational partial differential equation (PDE) based level set method for simultaneous image segmentation and registration is presented with an application to two-chamber human-heart end-systolic ultrasound images. The purpose of the model is to segment the endocardial borders of the given images using prior shape and intensity information. Prior shape and prior intensity of thirteen human-heart two-chamber end-systolic ultrasound images were generated by the method in Chen, Feng, et al. [12]. The segmentation is obtained by finding a non-rigid registration to the prior shape. The model performs a simultaneous segmentation and registration using an active contour approach similar to the one used by Chen, Yezzi, et al. [13, 15, 88]. But the model differs from Chen, Yezzi et al. [13, 15, 88] by using a shape prior as an initial contour. Since the shape prior is used as an initial contour, the level set form of the model is fixed which does not require the re-initialization process during the numerical calculation. The model in this Chapter is similar to the one used by Chen, Leventon, et al. [12, 13, 41], since it uses both prior shape and prior intensity information. However the segmentation in our model is obtained by finding the non-rigid deformation to the prior shape. The model in this Chapter follows the idea from Paragios, Metaxas, Yezzi, et. al. [31, 32, 63, 64, 71] for matching nonequivalent shapes by the combination of a global rigid transformation and a local non-rigid deformation. However, the model differs from Paragios [63, 64] by having an intensity matching term in the energy function which provides the difference of the intensity variation across the prior

shape and the shape of interest. Minimizing the difference of the gradients of the intensity between a smoothed prior image and a smoothed given image is more accurate than minimizing the gradient term in the given image, due to the loss of the information of the gradient near the edge of the desired object.

Chapter 2 is organized as follows: active contour is reviewed briefly in section 2.2. Generate prior shape and intensity information is explained in section 2.3. In section 2.4, the model is proposed for a simultaneous segmentation and non-rigid registration. The level set form of the proposed model and Euler-Lagrange equations of the level set form are described in section 2.5. In section 2.6, numerical methods pertaining to the model are explained. Experimental results of the model which were applied to human-heart two-chamber end-diastolic ultrasound images are also shown in section 2.7. Alternate ways to create prior mean shape and clustering using various statistical methods are shown in section 2.8.

2.2 Background Review; Active Contours

Active contours are used to control the smoothness of the curve and to attract the contour towards the boundary of the object, especially they are used for image segmentation which is finding object boundaries in images. In this section, edge-based active contour models are briefly reviewed:

Let Ω in R^2 be a closed and bounded region of the plane and $I : \Omega \rightarrow R$ be an image defined on Ω. Let $C(p) = (x(p), y(p))(p \in [0, 1])$ be a differentiable parameterized curve in Ω. Kass, et al. [33] proposed the classical snake model which is formulated by minimizing the energy function:

$$\int_0^1 |C'(p)|^2 dp - \lambda \int_0^1 |\nabla I(C(p))| dp. \tag{2–1}$$

The first term in Equation (2-1) is called the internal energy and is used to control the smoothness of the curve. The second term is the external energy and is used to attract the contour towards the boundary of the object.

The following geometric deformable contour model based on the level set interpretation of the Euclidean curve was proposed by Caselles, Malladi, et al. [7, 8, 47]:

$$u_t = g(|\nabla I|)|\nabla u|(div(\frac{\nabla u}{|\nabla u|}) + \nu), \tag{2–2}$$

where $g(|\nabla I|)$ can be chosen as

$$g(|\nabla I|) = \frac{1}{1 + \beta|\nabla(G_\sigma * I)|^2},$$

where $\beta > 0$ and $\nu \geq 0$ are parameters, $G_\sigma(x) = \frac{1}{\sigma}e^{-\frac{|x|^2}{4\sigma}}$, so that $g(|\nabla I|)$ is strictly positive in homogeneous regions and near zero on the edges proposed by Caselles, Cootes, Yezzi, et al. [8, 17, 86]. In this formation, the evolving contour is the zero level set $(u(x, y, t) = 0)$ of the solution of Equation (2-2). The level set formulation is an improvement on the original because it can handle multiple contours and topological changes.

A further modification called geometric active contour model was proposed by Caselles, Kichenassamy, et al. [8, 38]. The main modification was to propose an image gradient dependent Riemannian arc length function for the contour. The arc length was taken to be the "energy" $E(C)$ of the contour and was designed in such a way that minimizing it leads to active contour becoming stationary at pixels of high gradient:

$$E(C) = \int_0^1 g(|\nabla I|)(C(p))|C'(p)|dp, \tag{2–3}$$

where $g(|\nabla I|)$ is the function defined in Equation (2-3). Because of the change of arc-length measure term $|C'(p)|dp$, the model does not depend on the choice of the parameters any more.

2.3 Generating Prior Shape and Intensity information

The purpose of our suggested model is to capture the boundary of the given images by using the prior shape and prior intensity information. It has been shown that prior mean shape can play an important role to acquire better segmentation results presented by Chen, leventon, Paragios, Yezzi, Duncan, et al. [12, 13, 14, 15, 41, 42, 63, 64. 71, 85]. Prior shape and prior intensity in our model were generated by the method in Chen, Feng, et al. [12] with an application to thirteen human-heart two-chamber epicardium ultrasound images. The followings are brief descriptions of the method to generate the prior mean shape and clustering from Chen, Feng, et al. [12] :

2.3.1 Area Difference Distance Measurement

There are several different ways to define the distance between two contours. The area difference distance measurement is used from Chen, et al. [16] to get the distance between two contours. The following is the brief review of the area distance and the model developed in Chen, et al. [16]:

The notion of shape in our model is assumed independent of translation, rotation, and scaling.

Definition 1. Let A and B be two contours. Then area(A, B) = the area of $(Int(A) \cup Int(B) - Int(A) \cap Int(B))$, where the "area" of digitized curves is defined and computed as in Chen et al. [16].

Definition 2. The area distance between two contours A and B is defined as the minimum area between two contours after rotation, translation, and scaling.

$$AD(A, B) := \min_{\mu, R, T}(area(\mu RA + T, B)) \tag{2-4}$$

In this subsection, we will denote $\mu R = \tilde{R} = \begin{bmatrix} a & -b \\ b & a \end{bmatrix}$.

Theorem 1. Let $A = (a_{ij})$, $B = (b_{ij})$, *and* $c_i = (b_{i+1,2} - b_{i,2})^2 + (b_{i+1,1} - b_{i,1})^2$, where $i = 1, \ldots, n$ and $j = 1,2$. Then

$$\min_{\tilde{R},T}(area(\tilde{R}A + T, B))$$

is achieved at $\tilde{R} = \begin{bmatrix} a & -b \\ b & a \end{bmatrix}$, $T = \begin{bmatrix} t_1 \\ t_2 \end{bmatrix}$, where

$$\begin{bmatrix} C1 & 0 & C2 & C3 \\ 0 & C1 & -C3 & C2 \\ C2 & -C3 & C4 & 0 \\ C3 & C2 & 0 & C4 \end{bmatrix} \begin{bmatrix} a \\ b \\ t_1 \\ t_2 \end{bmatrix} = \begin{bmatrix} B1 \\ B2 \\ B3 \\ B4 \end{bmatrix}, \tag{2–5}$$

$$C1 = \sum_{i=1}^{n} c_i(a_{i1}^2 + a_{i2}^2), \quad C2 = \sum_{i=1}^{n} c_i a_{i1}, \quad C3 = \sum_{i=1}^{n} c_i a_{i2}, \quad C4 = \sum_{i=1}^{n} c_i,$$

$$B1 = \sum_{i=1}^{n} c_i(b_{i1}a_{i1} + b_{i2}a_{i2}), \quad B2 = \sum_{i=1}^{n} c_i(b_{i2}a_{i1} - b_{i1}a_{i2}),$$

$$B3 = \sum_{i=1}^{n} c_i b_{i1}, \quad B4 = \sum_{i=1}^{n} c_i b_{i2}.$$

Here, $area(\tilde{R}A + T, B)$ was approximated by

$$\sum_{i=1}^{n} c_i((aa_{i1} - ba_{i2} + t_1 - b_{i1})^2 + (ba_{i1} + aa_{i2} + t_2 - b_{i2})^2).$$

2.3.2 Generating Prior Mean Shape and Clustering

The method to generate prior mean shape and clustering proposed by Chen, et al. [16] is briefly reviewed. To get the prior mean shape, first choose the first one of given n contours as an initial mean shape. Then align the rest of contours to an initial contour to obtain $\tilde{R}_1, \ldots, \tilde{R}_n$, and $T_1, \ldots, T_n$ using the area difference distance measurement from section 2.3.1. Finally, the prior mean shape C^* is

created by

$$C^* = (C_1 + \sum_{j=2}^{n} \tilde{R}_j C_j + T_j)/n. \tag{2-6}$$

If given contours have large shape variations, it is necessary to have a clustering process to obtain better prior mean shape. If the n training contours C_j, $j = 1, \ldots, n$ are to be grouped into k clusters, take k arbitrary contours as the initial contours. For the first cluster, fix an arbitrary contour, say C_1. Then align the rest of the contours to C_1 using Equation (2-4) to obtain $\tilde{R}_j C_j + T_j$, correspondingly $AD(C_1, C_j), j = 1, \ldots, n-1$. Define

$$\sigma = \sum_{j=2}^{n} AD(C_1, C_j)/(n-1). \tag{2-7}$$

Then the first cluster consists of all the curves C_k, such that $AD(C_1, C_k) < \sigma/3$. The remaining contours are grouped into $k-1$ clusters by repeating the above process. A prior intensity information image is created by using mutual information of image geometry. The details can be found in Chen, Huang, et al. [12]. These algorithms are tested against eighty-five two-chamber end-systolic endocardial human-heart cardiac borders. These contours are grouped into three clusters. The algorithms to generate prior mean shape and intensity information is tested against one of the clusters which has thirteen contours. Prior mean shape and intensity information of these thirteen contours and their corresponding images are created using the method from Chen, Feng, et al. [12]. Prior mean shape C^* and intensity information I^* of these thirteen contours and their corresponding images which have $0.62mm$ resolution in each pixel are created. The prior intensity information and a prior shape as a solid line are in Figure 2-1.

2.4 Description of the Proposed Model

The purpose of our model is to capture the boundary of the given image by using the prior shape and prior intensity information. Our prior shape and prior intensity of thirteen human-heart two-chamber epicardial ultrasound images were

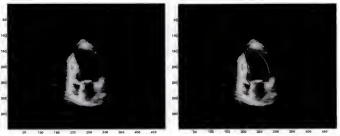

(a) (b)

Figure 2–1: (a)A Prior Intensity I^* (b)A Prior Shape C^* as a Solid Line

generated by the method from Chen , Huang et al. [12]. The model is proposed as follows:

Find a, u, v, μ, R, T by minimizing the energy function

$$\begin{aligned} E(a,u,v,\mu,R,T) = \lambda_1 \int_{N(C^*)} |\nabla(G_\sigma * I^*)(x,y) - a\nabla(G_\sigma * I)(\tilde{u},\tilde{v})|^2 d\bar{x} \\ +\lambda_2 \int_{N(C^*)} (|u|^2 + |v|^2) d\bar{x} + \lambda_3 \int_{N(C^*)} (|\nabla u|^2 + |\nabla v|^2) d\bar{x} \\ +\lambda_4 \int_0^1 g(|\nabla I|)(\tilde{u},\tilde{v})(C^*(p))|(C^*)'(p)|dp, \end{aligned} \tag{2–8}$$

$g(|\nabla I|)$ can be chosen as $g(|\nabla I|) = \frac{1}{1+\beta|\nabla(G_\sigma * I)|^2}$, $\beta > 0$ is a parameter, $G_\sigma(x) = \frac{1}{\sigma} e^{-\frac{|x|^2}{4\sigma}}$, and $\begin{bmatrix} \tilde{u}(x,y) \\ \tilde{v}(x,y) \end{bmatrix} = \mu R \begin{bmatrix} x \\ y \end{bmatrix} + T + \begin{bmatrix} u(x,y) \\ v(x,y) \end{bmatrix}$. An average image I^*, an original image I, and the average curve C^* are given and λ_1,λ_2, λ_3, and λ_4 are parameters. $N(C^*)$ is the neighborhood of the prior shape C^* and a, μ, R, and T are constants.

The first term minimizes the difference of the intensity variation across the prior shape and the shape of interest. Minimizing the difference of gradients of the intensity between smoothed prior image and the smoothed given image is more accurate than minimizing the gradient term in the given image, due to the loss of the information of the gradient near the edge of the desired object. Since images may have different levels of intensity, the model is also minimized over the scale factor variable a. The second term is minimizing the magnitude of the non-rigid

deformation term $\begin{bmatrix} u \\ v \end{bmatrix}$. Smoothing the non-rigid term $\begin{bmatrix} u \\ v \end{bmatrix}$ is in the third term. Final term is the energy functional of active contours proposed by Caselles, Yezzi, et al. [8, 38], that measures the amount of high gradient under the trace of the curve and increases the attraction of the evolving curve toward the boundary of the object. Since the prior shape C^* is used as an initial contour and the domain is taken as the neighborhood of the prior shape, it helps the numerical solutions converge faster. In addition, when the model is formulated into the level set form in Equation (2-9), the level set of the active contour in this model is fixed. Therefore, the re-initializing process in the calculation is not needed which decreases the numerical calculation time. In this model, a simultaneous segmentation and non-rigid registration is performed. The segmentation is obtained by finding a non-rigid registration to the prior shape. A registration consists of a global rigid transformation and a local non-rigid deformation.

2.5 Level Set Formulation of the Proposed Model

2.5.1 Level Set Formulation

The level set methods proposed by Osher, Sethian, et al. [59] are extensively used in the problems of curve evolution, because they allow the curve to develop cusps, corners, and topological changes. Now we give a variational level set approach proposed by Chan, Vese, Osher, et al. [9, 91] :

Let the contour C be the zero level set of a Lipschitz function w such that $\{x|w(x) > 0\}$ is the set inside C. Let $H(z)$ be the Heaviside function, that is $H(z) = 1$ if $z \geq 0$, and $H(z) = 0$ if $z < 0$, and $\delta = H'(z)$(in the sense of distribution) be the Dirac measure. Then, the length of the zero level set of u in the conformal metric $ds = g|C'(p)|dp$ can be measured by $\int_\Omega g(|\nabla H(w)|) = \int_\Omega \delta(w) g(|\nabla w|)$, where Ω is the image domain. Therefore, the level set formulation of our variational approach is to find a, u, v, μ, R, T by minimizing the energy

function

$$E(a,u,v,\mu,R,T) = \lambda_1 \int_{N(C^*)} |\nabla(G_\sigma * I^*)(x,y) - a\nabla(G_\sigma * I)(\tilde{u},\tilde{v})|^2 d\bar{x} + \lambda_2 \int_{N(C^*)} (|u|^2 + |v|^2) d\bar{x} + \lambda_3 \int_{N(C^*)} (|\nabla u|^2 + |\nabla v|^2) d\bar{x} + \lambda_4 \int_{N(C^*)} \delta(d_{C^*}) g(|\nabla I|)(\tilde{u},\tilde{v}) |\nabla d_{C^*}| d\bar{x}, \quad (2\text{–}9)$$

where d_{C^*} is the distance function of the average curve C^*, $g(|\nabla I|)$ can be chosen as $g(|\nabla I|) = \frac{1}{1+\beta|\nabla(G_\sigma * I)|^2}$, $\beta > 0$ is a parameter, $G_\sigma(x) = \frac{1}{\sigma} e^{-\frac{|x|^2}{4\sigma}}$, and $\begin{bmatrix} \tilde{u}(x,y) \\ \tilde{v}(x,y) \end{bmatrix} = \mu R \begin{bmatrix} x \\ y \end{bmatrix} + T + \begin{bmatrix} u(x,y) \\ v(x,y) \end{bmatrix}$. An average image I^*, an original image I, and the average curve C^* are given and λ_1,λ_2, λ_3, and λ_4 are parameters.

2.5.2 Euler-Lagrange Equations:

The evolution equations associated with the Euler-Lagrange equations of (2-9) are

$$\frac{\partial a}{\partial t} = \lambda_1 \int_{N(C^*)} (\nabla(G_\sigma * I^*)(x,y) - a\nabla(G_\sigma * I)(\tilde{u},\tilde{v}))(\nabla(G_\sigma * I)(\tilde{u},\tilde{v}))d\bar{x} \quad (2\text{–}10)$$

$$\frac{\partial u}{\partial t} = \lambda_1(\nabla(G_\sigma * I^*)(x,y) - a\nabla(G_\sigma * I)(\tilde{u},\tilde{v}))a(\frac{\partial(\nabla(G_\sigma * I)(\tilde{u},\tilde{v}))}{\partial \tilde{u}}) - \lambda_2 u + \lambda_3 \Delta u - \lambda_4 \delta(d_{C^*})(\frac{\partial g(|\nabla I|)(\tilde{u},\tilde{v})}{\partial \tilde{u}})|\nabla d_{C^*}|, \quad in\ N(C^*)$$
$$\frac{\partial u}{\partial n} = 0, \quad on\ \partial N(C^*) \quad (2\text{–}11)$$

$$\frac{\partial v}{\partial t} = \lambda_1(\nabla(G_\sigma * I^*)(x,y) - a\nabla(G_\sigma * I)(\tilde{u},\tilde{v}))a(\frac{\partial(\nabla(G_\sigma * I)(\tilde{u},\tilde{v}))}{\partial \tilde{v}}) - \lambda_2 v + \lambda_3 \Delta v - \lambda_4 \delta(d_{C^*})(\frac{\partial g(|\nabla I|)(\tilde{u},\tilde{v})}{\partial \tilde{v}})|\nabla d_{C^*}|, \quad in\ N(C^*)$$
$$\frac{\partial v}{\partial n} = 0, \quad on\ \partial N(C^*) \quad (2\text{–}12)$$

$$\frac{\partial \mu}{\partial t} = \lambda_1 \int_{N(C^*)} (\nabla(G_\sigma * I^*)(x,y) - a\nabla(G_\sigma * I)(\tilde{u},\tilde{v}))$$

$$a(\frac{\partial(\nabla(G_\sigma * I)(\tilde{u},\tilde{v}))}{\partial \tilde{u}} + \frac{\partial(\nabla(G_\sigma * I)(\tilde{u},\tilde{v}))}{\partial \tilde{v}})R \begin{bmatrix} x \\ y \end{bmatrix} d\bar{x} -$$

$$\lambda_4 \int_{N(C^*)} \delta(d_{C^*})(\frac{\partial g(|\nabla I|)(\tilde{u},\tilde{v})}{\partial \mu})R \begin{bmatrix} x \\ y \end{bmatrix} |\nabla d_{C^*}| d\bar{x} \tag{2–13}$$

$$\frac{\partial \theta}{\partial t} = \lambda_1 \int_{N(C^*)} (\nabla(G_\sigma * I^*)(x,y) - a\nabla(G_\sigma * I)(\tilde{u},\tilde{v}))$$

$$a(\frac{\partial(\nabla(G_\sigma * I)(\tilde{u},\tilde{v}))}{\partial \tilde{u}} + \frac{\partial(\nabla(G_\sigma * I)(\tilde{u},\tilde{v}))}{\partial \tilde{v}})\frac{dR}{d\theta} \begin{bmatrix} x \\ y \end{bmatrix} \mu d\bar{x} -$$

$$\lambda_4 \int_{N(C^*)} \delta(d_{C^*})(\frac{\partial g(|\nabla I|)(\tilde{u},\tilde{v})}{\partial \mu})\frac{dR}{d\theta} \begin{bmatrix} x \\ y \end{bmatrix} \mu |\nabla d_{C^*}| d\bar{x} \tag{2–14}$$

$$\frac{\partial T}{\partial t} = \lambda_1 \int_{N(C^*)} (\nabla(G_\sigma * I^*)(x,y) - a\nabla(G_\sigma * I)(\tilde{u},\tilde{v}))$$

$$a(\frac{\partial(\nabla(G_\sigma * I)(\tilde{u},\tilde{v}))}{\partial \tilde{u}} + \frac{\partial(\nabla(G_\sigma * I)(\tilde{u},\tilde{v}))}{\partial \tilde{v}}) d\bar{x} -$$

$$\lambda_4 \int_{N(C^*)} \delta(d_{C^*})(\frac{\partial g(|\nabla I|)(\tilde{u},\tilde{v})}{\partial T})|\nabla d_{C^*}| d\bar{x}, \tag{2–15}$$

where R is the rotation matrix in terms of the angle θ.

2.6 Numerical Methods

In this section, we explain how to solve the equations (2-10)-(2-15) numerically. Equation (2-9) was solved by finding a steady state solution of (2-10)-(2-15). Following the approach presented by Chan, Vese, et al. [9], we replace H and δ in

(2-10)-(2-15) by the regularized versions of them, denoted

$$H_\varepsilon(z) = \begin{cases} 1, \ if \quad z > \varepsilon \\ 0, \ if \quad z \leq -\varepsilon \\ \frac{1}{2}[1 + \frac{z}{\varepsilon} + \frac{1}{\pi} sin(\frac{\pi z}{\varepsilon})], \ if \quad |z| \leq \varepsilon, \end{cases}$$

and,

$$\delta_\varepsilon(z) = H'_\varepsilon(z) = \begin{cases} 0, \ if \quad |z| > \varepsilon \\ \frac{1}{2\varepsilon}[1 + cos(\frac{\pi z}{\varepsilon})], \ if \quad |z| \leq \varepsilon, \end{cases}$$

To discretize the equations (2-10)-(2-15), we use a finite difference scheme and we applied the gradient descent method. Let u_{ij} denote the value of u at the pixel $x_i = ih$ and $y_j = jk$, where h and k is the pixel size. Denote $u(x_i, y_j, t_n)$ by u^n_{ij}. The time derivative u_t at (i, j, t_n) is approximated by the forward difference scheme:

$$u_t(i, j, t_n) = \frac{u^{n+1}_{ij} - u^n_{ij}}{\Delta t},$$

where Δt is the time step. Moreover, (2-10)-(2-15) were implemented by the following iteration scheme :

$$(u_x)^n_{ij} = \frac{u^n_{(i+1)j} - u^n_{ij}}{h}, \quad (u_y)^n_{ij} = \frac{u^n_{i(j+1)} - u^n_{ij}}{k},$$

$$(u_{xx})^n_{ij} = \frac{u^n_{(i+1)j} - 2u^n_{ij} + u^n_{(i-1)j}}{h^2}, \quad (u_{yy})^n_{ij} = \frac{u^n_{i(j+1)} - 2u^n_{ij} + u^n_{i(j-1)}}{k^2},$$

$$((G_\sigma * I^*)_x)^n_{ij} = \frac{(G_\sigma * I^*)^n_{(i+1)j} - (G_\sigma * I^*)^n_{ij}}{h},$$

$$((G_\sigma * I^*)_y)^n_{ij} = \frac{(G_\sigma * I^*)^n_{i(j+1)} - (G_\sigma * I^*)^n_{ij}}{k},$$

$$((G_\sigma * I)_x)^n_{ij} = \frac{(G_\sigma * I)^n_{(i+1)j} - (G_\sigma * I)^n_{ij}}{h},$$

$$((G_\sigma * I)_y)^n_{ij} = \frac{(G_\sigma * I)^n_{i(j+1)} - (G_\sigma * I)^n_{ij}}{k},$$

$$(g(|\nabla I|)_x)^n_{ij} = \frac{g(|\nabla I|)^n_{(i+1)j} - g(|\nabla I|)^n_{ij}}{h},$$

$$(g(|\nabla I|)_y)_{ij}^n = \frac{g(|\nabla I|)_{i(j+1)}^n - g(|\nabla I|)_{ij}^n}{k}.$$

2.7 Experimental Results

It is very difficult to segment human-heart cardiac borders, due to significant signal loss, noise, and non-uniformity of regional intensities in ultra sound images. The purpose of the model is to segment two-chamber end-systolic endocardial human-heart ultrasound images using a prior shape and a prior intensity profile.

Feng, Chen, et al. developed an algorithm to generate a prior mean shape by clustering extracted from eighty-five two-chamber end-systolic endocardial human-heart cardiac borders. These eighty-five contours were grouped into three clusters. The proposed model is tested against the mean contour from the cluster which contained thirteen contours. Prior mean shape C^* and intensity information I^* of these thirteen contours and their corresponding images which have $0.62mm$ resolution in each pixel are created by using the method in section 2.3.1 and 2.3.2. For the details, refer to Chen, Huang, et al. [12]. The prior intensity information and a prior shape are in Figure 2-1. The left image in Figure 2-1 represents the average image as prior intensity information. The solid line in the right image in Figure 2-1 is the average curve as a prior shape.

To show the effectiveness of the local non-rigid deformation term in the model, a global rigid transformation model is created without non-rigid deformation term $\begin{bmatrix} u \\ v \end{bmatrix}$ in Equation (2-9). Numerical calculation is done without the non-rigid term. To validate experimental results of the model, distance measurements from the results of the model with non-rigid term from expert's borders from Figure 2-4 to Figure 2-7 are followed in the Table 2-2. Distance measurements to the results of the model with rigid term only from expert's borders from Figure 2-4 to Figure 2-7 are presented in the Table 2-3. Tables 2-2 and 2-3 provide the effectiveness of the proposed model.

In Figures (a) 2-2, 2-4, 2-5, 2-6, and 2-7, a solid line is the initial contour in a novel image. A prior shape is used as an initial contour. From Figure 2-2 to Figure 2-3, the effectiveness of each term is shown in the model. The solid line from Figure 2-2 to Figure 2-3 is the proposed model result with special condition of λ_i, where $i = 1, 2, 3, 4$. The expert endocardial border is compared as a dotted line. Figure (b) in 2-2 shows the model performance with $\lambda_1 = 0$ and the distance measurement from expert's border is $29.1537(18.7529mm)$. Figure (c) in 2-2 shows the model performance with $\lambda_2 = 0$ and the distance measurement from expert's border is 2.4027 $(1.4897mm)$. Figure (a) in (2-3) shows the model performance with $\lambda_3 = 0$ and the distance measurement from expert's border is 9.7669 $(6.0555mm)$. Figure (b) in (2-3) shows the model performance with $\lambda_4 = 0$ and the distance measurement from expert's border is 1.8930 $(1.1737mm)$. From Table 2-1, it is easily seen that the major contribution terms in the model are the first and third terms. From Figure 2-4 to Figure 2-7, the model comparisons between the local non-rigid term and without the local non-rigid term. For Figure (b) in (2-4) to (2-7), the solid line is the model's result with the local non-rigid deformation term. The expert endocardial border is represented by a dotted line. For Figure (c) in 2-4 to 2-7, the solid line is the result of the model without a local non-rigid deformation term in the Equation (2-9). In a similar way, the expert endocardial border is represented as a dotted line. From the Figures and the distance measurement results from the expert' border in Table 2-2 and Table 2-3, it is easily seen that the performance of the suggested model is better than the model without a local non-rigid deformation in the Equation (2-9). In Figure 2-4, the distance result from the model with non-rigid term is $1.8442(1.1434mm)$ which is better than the distance result $2.2160(1.3739mm)$ from the global rigid transformation model. In Figure 2-5, the distance result from the model with non-rigid term is $1.8431(1.1427mm)$ which is better than the distance result

1.9670(1.2195mm) from the global rigid transformation model. In Figure 2-6, the distance result from the model with non-rigid term is 2.2301(1.3826mm) which is better than the distance result 2.8891(1.7912mm) from the global rigid transformation model. In Figure 2-7, the distance result from the model with non-rigid term is 2.0686(1.2825mm) which is better than the distance result 3.0470(1.8891mm) from the global rigid transformation model. Since the local deformation is assumed small in the model, the distance difference between the model with non-rigid term and the global rigid transformation only model is not big. However, Table 2-2 and Table 2-3 shows the effectiveness of the suggested model. Finally, Table 2-4 and Table 2-5 presented the parameters which were chosen as examples where accurate results of the proposed model were obtained.

During the numerical experiments, the parameters λ_i, $i = 1, 2, 3, 4$ are estimated by trial and error basis. There are several different ways to estimate unknown parameters. One of the approaches is to incorporate unknown parameters into the energy function. Then find steady state solutions of Euler-Lagrange equations involved with these parameters. Statistical approaches have been also developed to get best estimation of unknown parameters. The estimation of parameters can be presented in Gauss-Markoff model and several approaches including least squares method and maximum-likelihood method have been proposed to estimate Gauss-Markoff model. For the details, refer to [39].

A standard technique to estimate parameters in our proposed model is introduced. First, fix one parameter, say $\lambda_4 = 1$. If we have a training set of n contours and images from the expert, follow the procedure from section 2.3 to get prior shape and intensity information. Then a, u, v, μ, R, T can be measured using the discretized solutions of Equations (2-10) through (2-15). Hence n energy functions $E_i(a_i, u_i, v_i, \mu_i, R_i, T_i) = 0$, $i = 1, 2, \ldots, n$ are formed. This process results in the following matrix equation :

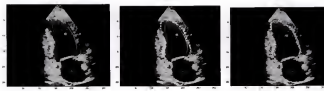

(a) (b) (c)

Figure 2–2: Subject 2 : Solid Line by Our Model Result and Dotted Line by Expert (a)A Initial Contour, (b) Model with $\lambda_1 = 0$, (c) Model with $\lambda_2 = 0$

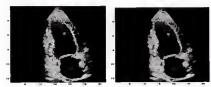

(a) (b)

Figure 2–3: Subject 2 : Solid Line by Our Model Result and Dotted Line by Expert (a) Model with $\lambda_3 = 0$, (b) Model with $\lambda_4 = 0$

$$\begin{bmatrix} A_{11} & A_{12} & A_{13} \\ A_{21} & A_{22} & A_{23} \\ \cdots & \cdots & \cdots \\ A_{n1} & A_{n2} & A_{n3} \end{bmatrix} \begin{bmatrix} \lambda_1 \\ \lambda_2 \\ \lambda_3 \end{bmatrix} = \begin{bmatrix} B_1 \\ B_2 \\ \cdots \\ B_n \end{bmatrix}, \tag{2–16}$$

where $A_{i1} = \int_{N(C^*)} |\nabla((G_\sigma)_i * I^*)(x,y) - a\nabla((G_\sigma)_i * I)(\vec{u}_i, \vec{v}_i)|^2 d\vec{x}$, $A_{i2} = \int_{N(C^*)} (|u_i|^2 + |v_i|^2) d\vec{x}$, $A_{i3} = \int_{N(C^*)} (|\nabla u_i|^2 + |\nabla v_i|^2) d\vec{x}$, and $B_i = -\int_{N(C^*)} \delta(d_{C^*}) g_i(|\nabla I|)(\vec{u}_i, \vec{v}_i) |\nabla d_{C^*}| d\vec{x}$, $i = 1, 2, \ldots, n$.

Denote $A := \begin{bmatrix} A_{11} & A_{12} & A_{13} \\ A_{21} & A_{22} & A_{23} \\ \cdots & \cdots & \cdots \\ A_{n1} & A_{n2} & A_{n3} \end{bmatrix}$, $\lambda := \begin{bmatrix} \lambda_1 \\ \lambda_2 \\ \lambda_3 \end{bmatrix}$, and $B := \begin{bmatrix} B_1 \\ B_2 \\ \cdots \\ B_n \end{bmatrix}$. Then multiply A^t to both sides of Equation (2-16). Find an inverse matrix of 3×3 matrix $A^t A$ and multiply to both sides to solve the equation $A^t A\lambda = A^t B$. Finally, desired λ_1, λ_2, and λ_3 are obtained.

Table 2–1: Distance Measurements of the Result of the Model from Expert's Borders from Figure 2-2 to Figure 2-3

Terms in Model	(a)Initial	(b)Result
Subject 2 with $\lambda_1 = 0$	29.1273(18.0589mm)	29.1537(18.0753mm)
Subject 2 with $\lambda_2 = 0$	29.1273(18.0589mm)	2.4027 (1.4897mm)
Subject 2 with $\lambda_3 = 0$	29.1273(18.0589mm)	9.7669 (6.0555mm)
Subject 2 with $\lambda_4 = 0$	29.1273(18.0589mm)	1.8930 (1.1737mm)

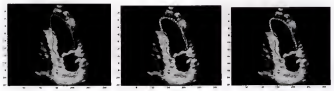

(a) (b) (c)

Figure 2–4: Subject 1 : Solid Line by Our Model Result and Dotted Line by Expert (a)An Initial Contour (b) Model with Non-Rigid Term, (c) Model with Rigid Term Only

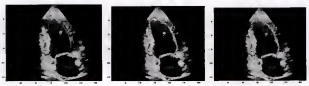

(a) (b) (c)

Figure 2–5: Subject 2 : Solid Line by Our Model Result and Dotted Line by Expert (a)An Initial Contour (b) Model with Non-Rigid Term, (c) Model with Rigid Term Only

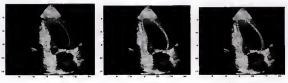

(a) (b) (c)

Figure 2–6: Subject 3 : Solid Line by Our Model Result and Dotted Line by Expert (a)An Initial Contour (b) Model with Non-Rigid Term, (c) Model with Rigid Term Only

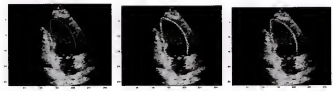

(a) (b) (c)

Figure 2–7: Subject 4 : Solid Line by Our Model Result and Dotted Line by Expert (a)An Initial Contour (b) Model with Non-Rigid Term, (c) Model with Rigid Term Only

Table 2–2: Distance Measurements of the Result of the Model with Non-Rigid Term from Expert's Borders from Figure 2-4 to Figure 2-7

Figures	(a)Initial	(b)Non-rigid term result
Subject 1	25.1354 (15.5839mm)	1.8442(1.1434mm)
Subject 2	29.1273(18.0589mm)	1.8431 (1.1427mm)
Subject 3	10.7297 (6.6524mm)	2.2301 (1.3826mm)
Subject 4	4.4458 (2.7563mm)	2.0686 (1.2825mm)

Table 2–3: Distance Measurements of the Result of the Model with Rigid Term Only from Expert's Borders from Figure 2-4 to Figure 2-7

Figures	(a)Initial	(b)Rigid term result
Subject 1	25.1354 (15.5839mm)	2.2160 (1.3739mm)
Subject 2	29.1273(18.0589mm)	1.9670 (1.2195mm)
Subject 3	10.7297 (6.6524mm)	2.8891 (1.7912mm)
Subject 4	4.4458 (2.7563mm)	3.0470 (1.8891mm)

Table 2-4: The Parameters Used for Figure 2-4 through Figure 2-7 with Non-Rigid Term

Figures	(a)$\lambda 1$	(b)$\lambda 2$	(c)$\lambda 3$	(d)$\lambda 4$
Subject 1	4.0	0.0001	500	100
Subject 2	0.2	0.0000001	500	100
Subject 3	0.2	0.0000001	500	100
Subject 4	0.5	0.0001	500	100

Table 2-5: The Parameters Used for Figure 2-4 through Figure 2-7 with Rigid Term Only

Figures	(a)$\lambda 1$	(b)$\lambda 2$	(c)$\lambda 3$	(d)$\lambda 4$
Subject 1	4.0	0	0	100
Subject 2	0.2	0	0	100
Subject 3	0.2	0	0	100
Subject 4	0.5	0	0	100

2.8 Generating Prior Mean Shape and Clustering

Shape analysis has become one of the most important and interesting areas and has a wide range of applications including pattern recognition, object recognition, and medical image analysis. Due to more advanced algorithmic models that better allow researchers to analyze images, shape analysis is now a major focus to many researchers who then attempt to employ mathematics, statistics, and many other computer aided techniques to further theoretical developments.

Central to the shape analysis problem is the notion of a random shape. Frechet [23] initiated developments of this area for analyzing the random shapes, e.g., curves. Matheron [52] and David Kendall [34, 35, 36] and his colleagues continued after him for mostly further theoretical developments of the analysis of random shapes.

The statistical analysis of shapes was initiated by Sir D'Arcy Wentworth Thompson [76]. A theory and practice for the statistical analysis for the shapes have been developed by Bookstein [4], Dryden and Mardia [20], Carne [6], Kent and Mardia [37], Cootes, Taylor and colleagues [18]. Their ideas are tied to the

old study of the point-wise representation of the shapes: objects are represented by a finite number of salient points or landmarks by Frechet [23], Matheron [52], and David Kendall [34, 35, 36]. The models in this paper follow the ideas similarly from Bookstein [4], Dryden and Mardia[20], Carne [6], Kent and Mardia [37], and Cootes, Taylor and colleagues [18] by studying the point-wise representation of the shapes using statistical methods.

One of the objectives of the shape analysis is to find the mean shape of the given contours by minimizing a shape related energy function. Mean shape plays an important role in image segmentation and registration and is used as prior information proposed by Chen, leventon, Paragios, Yezzi, Duncan, et al. [12, 13, 14, 15, 41, 42, 63, 64, 71, 85] to overcome difficulties which include significant signal loss, noise, and non-uniformity of regional intensities. To find the best representation of the given contours, several statistical methods have been developed including the Procrustes mean, Principal Component Analysis [73], and generalized orthogonal Procrustes analysis [73]. The suggested model is not only to create the mean shape but also to generate alignments between the mean shape and the given contours.

The other goal is to generate the mean shape and clustering of the given contours using the Self-Organizing map. For basic pattern recognition, the Self-Organizing map, which was developed by Professor Teuvo Kohonen in the early 1980s, is widely used and can be visualized as a sheet-like neural-network array, the cells (or nodes) of which become specifically turned to various input signal patterns or classes of patterns in an orderly fashion. The learning process is competitive and unsupervised, meaning that no training set of data is needed to define the correct output (or actually the cell into which the input is mapped) for an input. In the basic version, only one map node (winner) at a time is activated corresponding to each input. The details of the self organizing map can be found in [40].

To measure the similarities between the cells(or nodes), the Procrustes method can be applied. This technique was given a solid mathematical foundation in the seminal work of Kendall [35]. The Procrustes distance is a least-squares type shape metric that requires one to one correspondence between two aligned shapes. Several Procrustes methods have been developed including an area difference distance method and orthogonal Procrustes method. The orthogonal Procrustes alignment is calculated by a point-wise correspondence and there is no need for the re-parametrization process to obtain the correct correspondence between contours. Meanwhile, area difference measurement method needs to be re-parametrized to get the correct correspondence between contours in each iteration. Hence the orthogonal Procrustes method has an advantage of faster computation time than that of the area difference distance. In this dissertation, these two methods combined with Self-Organizing map are compared. In addition, the Self- Organizing map combined with Principal Component Analysis is presented to get better shape variations.

2.8.1 Generating Mean Shape with Orthogonal Procrustes Measurement

The model which minimizes a shape related energy function to create shape representation with the orthogonal Procrustes method is presented. This model does not depend upon the choice of the initial contour. The orthogonal Procrustes analysis finds the best alignment between two contours. Since the method is fairly simple and calculation time is fast, it is widely used. The followings are the brief review of the orthogonal Procrustes method presented by Stegmann and Gomez [73]:

2.8.1.1 Orthogonal Procrustes Method.

The Procrustes distance method is a least-square type shape metric that requires two aligned contours with one-to-one point correspondence. The method

was named from Procrustes(the subduer), son of Poseidon, who kept an inn benefiting from what he claimed to be a wonderful all-fitting bed. He lopped off excessive limbage from tall guests and either flattened short guests by hammering or stretched them by racking. The victim fitted the bed perfectly but, regrettably, died. To exclude the embarrassment of an initially exact-fitting guest, variants of the legend allow Procrustes two, different-sized beds. Ultimately, in a crackdown on robbers and monsters, the young Theseus fitted Procrustes to his own bed. The orthogonal Procrustes method is a least-square shape metric that requires two aligned shapes with one-to-one correspondence. The alignment part involves four steps :

STEP 1. Compute the centroid of each iteration.

STEP 2. Re-scale each shape to have equal size.

STEP 3. Align with respect to position the two shapes at their centroid.

STEP 4. Align with respect to orientation by rotation.

2.8.1.2 Description of the Suggested Model

A new model which minimizes a shape related energy function to create mean shape with the orthogonal Procrustes method is presented in this section. This model does not depend upon the choice of the initial contour. In addition, the model generates the mean shape and the alignments for the given shapes to this mean shape simultaneously. The symbol C^* is the mean shape of the given contours $C_1, \ldots, C_n$ and $R_1, \ldots, R_n$ are the rotation matrices with respect to the angle θ which brings the best fit to the mean shape from the given shapes, respectively. Here n is the total number of given contours. The model finds $C^*, R_1, \ldots, R_n$ by minimizing the energy functional :

$$E(C^*, R_1, \ldots, R_n) = \sum_{i=1}^{n} \|C^* - R_i C_i\|^2. \tag{2-17}$$

The Equation (2-17) was solved by finding a steady state solution of the evolution equations. The evolution equations are associated with the Euler-Lagrange equations of the Equation (2-17). Then apply the gradient descent method to the evolution equation to generate the mean shape C^*. Then use the orthogonal Procrustes method to get the best alignments between C^* and $C_1, \ldots, C_n$, respectively. This gives $R_1, \ldots, R_n$.

The iterative approach to the suggested algorithm is the following six steps :

STEP 1. Compute the centroid of each iteration.

STEP 2. Re-scale each shape to have equal size.

STEP 3. Choose an initial estimate of the mean shape (e.g. the arithmetic mean of the given n contours).

STEP 4. Align all the remaining shapes to the mean shape to get $R_1, \ldots, R_n$..

STEP 5. Recalculate the mean shape C^* by applying the gradient descent method to the evolution Equation of (2-17).

STEP 6. If the estimated mean has changed, return to STEP 4. In a similar way, convergence is obtained when the mean shape and the rotation matrix do not change within an iteration.

2.8.1.3 Experimental Results

The results of applications to the eighty-five human-heart two-chamber normal end-diastolic epicardiac borders traced by experts are shown. The purpose of the model is to generate the shape representation of the given set of contours by minimizing a shape related energy function. The model does not depend on the choice of the initial contour and generates the mean shape and alignments to the mean shape from the given contours simultaneously.

Verification of the results are done by three different measurements : mean distance, standard deviation, and Tanimoto measurement. Let $A_i, i = 1, 2, \cdots, n$ be given contours and M be an average shape of given contours. The mean distance

Figure 2–8: Left : A Initial Contour, Right : The Results are from the Shape Related Energy Function with the Mean Shape as a Dotted Line with 85 human-heart end-diastolic epicardial borders

is $\frac{\sum_{i=1}^{n} d(A_i,M)}{n}$, where d is a distance between A_i and M. The standard deviation is $\frac{\sum_{i=1}^{n} std(A_i,M)}{n}$, where $std(A_i,M)$ is a standard deviation between A_i and M. Finally, the Tanimoto distance is $\frac{\sum_{i=1}^{n} T_d(A_i,M)}{n}$, where $T_d = 1 - \frac{A_i \cdot M}{\|A_i\|^2 + \|M\|^2 - A_i \cdot M}$. This measurement is used to compare the dissimilarity of the given contours to an average shape. The details of the Tanimoto similarity measurement are presented by Kohonen [40].

Figure 2-8 represents the shape related energy function model result applied eighty-five human-heart end-diastolic epicardial borders. For Figure 2-8, a dotted line in the left one is the initial contour of the given contours. The dotted line in the right one is mean shape of the given contours. Three distance measurements, namely mean distance, standard deviation, and Tanimoto measurement of the result of the models from Figure 2-8 is in Table 2-6.

Table 2–6: Distance Measurements of the Result of the Models from Figure 2-8, n=85

Figure	(a)Mean Distance	(b)Standard Deviation	(b)Tanimoto Distance
Figure 2-20	0.0635	0.0535	0.0088

2.8.2 Generating Mean Shape and Clustering using Self-Organizing Map

2.8.2.1 Description of the Self-Organizing Map(SOM)

In this section, the Self-Organizing map is described. The following is the brief description of the Self-Organizing map from Kohonen and Honkela [30, 40]:

The set of input samples is described by a real vector $\mathbf{x}(t) \in R^n$, where t is the index of the sample, or the discrete-time coordinate. Decide number of clusters in advance, say k. Each clustering $i = 1, 2, \ldots, k$ in the map contains a model vector $\mathbf{m}_i(t) \in R^n$, which has the same number of elements as the input vector $\mathbf{x}(t)$. The stochastic Self-Organizing Map algorithm performs a regression process. Thereby, the initial values of the components of the model vector, $\mathbf{m}_i(t)$, may even be selected at random. Any input item is thought to be mapped into the location, the $\mathbf{m}_i(t)$ of which matches best with $\mathbf{x}(t)$ in some metric. The self-organizing algorithm creates the ordered mapping as a repetition of the following basic tasks: First, compare an input vector $\mathbf{x}(t)$ with all the model vectors $\mathbf{m}_i(t)$. Best-matching unit (node) on the map, i.e., the node where the model vector is most similar to the input vector in some metric (e.g. Euclidean) is identified. This best matching unit is often called the winner. Then, the model vectors of the winner and a number of its neighboring nodes in the array are changed towards the input vector according to the learning principle specified below. Adaptation of the model vectors in the learning process may take place according to the following equations:

$$\left[\begin{array}{l} \mathbf{m}_i(t+1) = \mathbf{m}_i(t) + \alpha(t)[\mathbf{x}(t) - \mathbf{m}_i(t)], if\ i \in N_c(t) \\ \mathbf{m}_i(t+1) = \mathbf{m}_i(t),\ otherwise, \end{array}\right] \tag{2–18}$$

where t is the discrete-time index of the variables, the factor $\alpha(t) \in [0, 1]$ is a scalar that defines the relative size of the learning step, and $N_c(t)$ specifies the neighborhood around the winner in the map array. At the beginning of the learning

process the radius of the neighborhood is fairly large, but it is made to shrink during learning. This ensures that the global minimum is obtained already at the beginning, whereas towards the end, as the radius gets smaller, the local corrections of the model vectors in the map will be more specific. The factor $\alpha(t)$ also decreases during learning.

2.8.2.2 Self-Organizing Map with Procrustes Methods

The purpose of the model is to generate the shape representation and classification of the given contours using the Self-Organizing map combined with the Procrustes methods. This technique has the advantage of generating shape representation of each cluster and classifying given contours simultaneously. In this section, the suggested model is explained. The following is the description of the proposed model:

STEP 1. First, centralize and normalize all the n training contours C_i. to get the equal length. If the n training contours C_i, $i = 1, \ldots, n$ to be grouped into k clusters, take k arbitrary contours as the initial contours, denoted by $m_j(0)$ $(j = 1, \ldots, k)$.

STEP 2. At $(t + 1)$ iteration, randomly select a contour denoted by $X(t + 1)$ from the training set, and compare the disparity in shape between $X(t + 1)$ and each of $m_j(t)$ $(j = 1, \ldots, k)$.

STEP 3. To do this comparison, align $X(t + 1)$ to each $m_j(t)$, and denote the aligned $X(t + 1)$ by $\tilde{X}_j(t + 1) = R_j X(t + 1) + T_j$.

STEP 4. Then we compute $A_j := AD(\tilde{X}_j(t + 1), m_j)$ by using the orthogonal Procrustes method in (2.8.1.1).

STEP 5. Suppose A_1 is the smallest number in A_j, $j = 1, ..., k$. Keep $m_2(t)$, $\ldots$, $m_k(t)$ unchanged, and update $m_1(t)$ by

$$m_1(t + 1) = m_1(t) + \alpha(t)[\tilde{X}_1(t + 1) - m_1(t)],$$

where $\alpha(t)$ is a smooth function of t, and decreases to zero as $t \to \infty$. Then normalize $m_1(t)$.

STEP 6. After a large number, say $t = N$, k *average* shapes $m_j(N)$ $(j = 1, \ldots, k)$ are generated.

STEP 7. Then k clusters are formed by the contours that are closest to the *average* shapes. The closeness is again measured by an orthogonal Procrustes measurement or area difference distance measurement.

2.8.2.3 Self-Organizing Map Combined with Principal Component Analysis

The purpose of this model is to generate the mean shape and clustering of the given contours using the Self-Organizing map combined with the Principal Component Analysis method. The method is very similar to Section (2.8.2.2). To get better results, the given contours are pre-aligned using the method in Section (2.8.1.1). Then the algorithm from Section (2.8.2.2) is applied. After that Principal Component Analysis is applied to each group of clusters. The following is the basic summary of the proposed model:

STEP 1. Pre-align the given contours by applying the orthogonal Procrustes algorithm from Section (2.8.1.1).

STEP 2. Apply the STEP 1. through STEP 7. from Section (2.8.2.2) to get the mean shape and clustering to the pre-aligned contours.

STEP 3. Update the mean shape and clustering of each group by applying the Principal Component Analysis.

2.8.2.4 Experimental Results

The results of applications to the eighty-five human-heart two-chamber normal end-diastolic epicardiac borders are shown. The model does not depend upon the choice of the initial contour and generates the mean shape and clustering from the given contours simultaneously.

Verification of the results are done by three different measurements; mean distance, standard deviation, and Tanimoto measurement. Let $A_i, i = 1, 2, \cdots, n$ be given contours and M be an average shape of given contours. The mean distance is $\frac{\sum_{i=1}^{n} d(A_i, M)}{n}$, where d is a distance between A_i and M. The standard deviation is $\frac{\sum_{i=1}^{n} std(A_i, M)}{n}$, where $std(A_i, M)$ is a standard deviation between A_i and M. Finally, the Tanimoto distance is $\frac{\sum_{i=1}^{n} T_d(A_i, M)}{n}$, where $T_d = 1 - \frac{A_i \cdot M}{\|A_i\|^2 + \|M\|^2 - A_i \cdot M}$. This measurement is used to compare the dissimilarity of the given contours to an average shape. The detail of the Tanimoto similarity measurement is in [40].

From Figure 2-9 to Figure 2-13 are the results which were obtained when this method was applied to the eighty-five human-heart two-chamber normal end-diastolic epicardiac borders to obtain clustering and the mean shape of each cluster. The self-organizing map is used. The closeness was measured by the area difference method or the orthogonal procrustes method. In the experiment, we use $\alpha(t) = 0.9(1 - t/N)$, where t is the time step and N is total number of iterations. The function α is smooth and decreases to zero as t approaches N. Figure 2-9 is the numerical results using Self-Organizing map with the area difference distance method. In a similar way, Figure 2-10 is the numerical results using Self-Organizing map with orthogonal Procrustes method. Since orthogonal Procrustes method is using one-to-one correspondence, we do not need the re-parameterizing process to find the correct correspondence which make the calculation time faster in each step than that of using area difference distance measurement. It is easily seen that the orthogonal method is more efficient than area difference method from Table 2-7. To get better mean shape, Figure 2-11 shows the numerical results using the method from section 2.8.2.3. Pre-alignments and applying principal component analysis give better results which can be easily seen in Table 2-7. From Figure 2-12 and Figure 2-13, numerical results with an application to the eighty-five human-heart two-chamber normal end-diastolic epicardiac borders to cluster into three

Figure 2–9: Two Chamber ED EPI Normal 85 Patients Heart Contours with 5000 Iterations using SOM + Area Difference Method. The Dotted Line Represents the Average of the Cluster with n=85

Figure 2–10: Two Chamber ED EPI Normal 85 Patients Heart Contours with 5000 Iterations using SOM + orthogonal Procrustes method. The Dotted Line Represents the Average of the Cluster with n=85

groups. Figure 2-12 shows the results using the method from section 2.8.2.2 with orthogonal Procrustes method. First group, there are 30 contours, 28 contours are in the second group. Finally 27 contours are in the third group. Numerical results using the method from section 2.8.2.3 is in Figure 2-13. Distance measurements comparisons from Table 2-8 and Table 2-9 show the effectiveness of the suggested models.

Figure 2–11: Two Chamber ED EPI normal 85 Patients Heart Contours with 5000 Iterations using SOM + PCA. The Dotted Line Represents the Average of the Cluster with n=85

Table 2–7: Distance Measurements of the Result of the Models from Figure 2-9 to Figure 2-11. M_d Represents Mean Distance. STD_d Represents Standard Deviation. T_d Represents Tanimoto Distance with n=85

Figures	(a)M_d	(b)STD_d	(c)T_d
Figure 2-21	0.4915	0.0504	0.7036
Figure 2-22	0.0063	0.0054	0.0082
Figure 2-23	0.0057	0.0051	0.0044

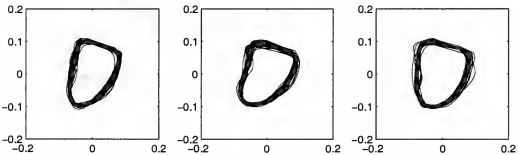

Figure 2–12: Two Chamber ED EPI Normal 85 Patients Heart Contours with 5000 Iterations into 3 Groups using SOM+Orthogonal Procrustes Measurement. The Dotted Line Represents the Average of the Cluster with n=85. Left : 30 contours, Middle : 28 contours, Right : 27 contours

Table 2–8: Distance Measurements of the Result of the Models from Figure 2-12. M_d Represents Mean Distance. STD_d Represents Standard Deviation. T_d Represents Tanimoto Distance

Groups	(a)M_d	(b)STD_d	(c)T_d
Group 1($n_1 = 30$)	0.0409	0.0128	0.0605
Group 2($n_2 = 28$)	0.0426	0.0128	0.0529
Group 3($n_3 = 27$)	0.0286	0.0103	0.0350

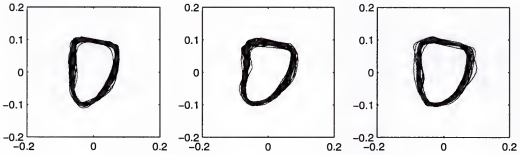

Figure 2–13: Two Chamber ED EPI Normal 85 Patients Heart Contours with 5000 Iterations using SOM + PCA. The Dotted Line represents the Average of the Cluster with n=85. Left : 30 contours, Middle : 28 contours, Right : 27 contours

Table 2–9: Distance Measurements of the Result of the Models from Figure 2-13. M_d Represents Mean Distance. STD_d Represents Standard Deviation. T_d Represents Tanimoto Distance

Groups	(a)M_d	(b)STD_d	(c)T_d
Group 1($n_1 = 30$)	0.0345	0.0098	0.0520
Group 2($n_2 = 28$)	0.0415	0.0101	0.0505
Group 3($n_3 = 27$)	0.0265	0.0097	0.0306

CHAPTER 3
A REGION-BASED MODEL FOR IMAGE SEGMENTATION AND REGISTRATION

3.1 Image Segmentation Using a Modified Mumford-Shah Technique

3.1.1 Introduction

Capturing the boundary of the given object is of primary importance in image processing, with applications to computer vision and medical imaging. Region based segmentation techniques have been developed by using the region statistics or homogeneity proposed by Chan, Vese, Cremers, Tsai, Mumford, Shah, Yezzi, Zhu, et al. [9, 10, 19, 22, 57, 75, 87, 93].

The most celebrated region based image segmentation model is introduced by Mumford and Shah in 1989 [57]. Using this model for a segmentation, an image is decomposed into a set of regions within the bounded open set Ω and these regions are separated by smooth edges Γ. Let $\Omega \subset R^n$ be a bounded domain with Lipschitz boundary and $u : \Omega \to R$. The model is formulated as a variational problem to minimize the following functional :

$$\min_{u,\Gamma} MS(u,\Gamma) = \lambda \int_{\Omega} (u - I)^2 d\bar{x} + \mu H(\Gamma) + \int_{\Omega \setminus \Gamma} |\nabla u|^2 d\bar{x}, \qquad (3\text{–}1)$$

where H stands for $(n-1)$ dimensional Hausdorff measure and λ and μ are parameters which balances three terms in the model. Here Γ is to be a closed subset of Ω given by the union of a finite number of curves. It represents the set of "edges" (i.e. boundaries of homogeneous regions) in the given image I. The function u is the piecewise smooth approximation to I. Because of the last term in Equation (3-1) taken over the set Ω/Γ, u is smooth in each connected component of Ω/Γ.

A simplification of Equation (3-1) is to find contour which separate two homogeneous regions with average intensity c_1 and c_2. This model is referred to as the piecewise constant Mumford-Shah model. Hence $u = c_1\mathbf{1}_\Gamma + c_2\mathbf{1}_{\Omega/\Gamma}$, where $\Gamma \subseteq \Omega$. In this case, Equation (3-1) reduces to the following minimization problem :

$$\min_{c_1,c_2,\Gamma} E(c_1, c_2, \Gamma) = \lambda \int_\Gamma (u - c_1)^2 d\bar{x} + \lambda \int_{\Omega/\Gamma} (u - c_2)^2 d\bar{x} + \mu Length(\Gamma), \qquad (3\text{–}2)$$

where λ and μ are parameters which balances three terms in the model. Model (3-2) is known as the two-phase, piecewise constant Mumford-Shah model. Chan and Vese [9] reformulate this model in the context of region based active contour :

$$\min_{c_1,c_2,\Gamma} E(c_1, c_2, \Gamma) = \lambda \int_{\Omega_+} (u - c_1)^2 d\bar{x} + \lambda \int_{\Omega_-} (u - c_2)^2 d\bar{x} + \mu Length(\Gamma), \qquad (3\text{–}3)$$

where Γ partitions Ω into interior Ω_+ and Ω_- and λ and μ are parameters which balances three terms in the model. Chan and Vese proposed a piecewise constant Mumford-Shah model in [9, 10] by using a level set formulation presented by Osher and Fedkiw [58]. In this approach, the boundary Γ is represented as the zero level set of a Lipschitz continuous function $\phi : \Omega \to R$. The purpose of this model is to express Equation (3-3) in terms of the level set function ϕ :

$$\min_{c_1,c_2,\Gamma} E(c_1, c_2, \Gamma) = \lambda \int_\Omega H(\phi)(u - c_1)^2 d\bar{x} + \lambda \int_\Omega (1 - H(\phi))(u - c_2)^2 d\bar{x} + \int_\Omega |\nabla H(\phi)| d\bar{x}, \qquad (3\text{–}4)$$

where λ is a parameter which balances three terms in the model and $H(\phi) : R \to R$ is the Heaviside function such that

$$H(\phi) := \begin{cases} 0, & if\ \phi < 0, \\ 1, & if\ \phi \geq 0. \end{cases}$$

Multiphase frameworks have also been developed by Chan and Vese [79]. Developments of variational level set implementation techniques based Mumford-Shah model are followed by Esedoglu, Gibou, Likar, et al. [22, 26, 43].

In the theory of Γ-convergence [1, 21, 49], the measuring an edge Γ length term in the Mumford-Shah model can be approximated by a quadratic integral of an edge signature function $p(x)$ such that

$$\int_{\Omega}(\epsilon|\nabla p|^2+\frac{(1-p)^2}{4\epsilon})d\bar{x}, \epsilon \ll 1$$

by Ambrosio and Tortorelli in 1990 [1]. The segmentation is represented by characteristic function using phase fields in Esedoglu, Likar, et al. [22, 43]. A diffuse interface approximation for Equation (3-2) proposed by Esedoglu, et al. [22] is given by the following sequence of energies :

$$MS_{\varepsilon}(u,c_1,c_2)=\int_{\Omega}\varepsilon|\nabla u|^2+\frac{1}{\varepsilon}W(u)+\lambda\{u^2(I-c_1)^2+(1-u)^2(I-c_2)^2\}d\bar{x}, \quad (3\text{–}5)$$

where $\varepsilon > 0$, λ is a parameter, u is the characteristic function, and the potential $W(u) = u^2(1-u)^2$. This potential function improves sharpness of edges. The details of phase field theory can be found in Baldo, Modica, Shen, Zhou, et al. [3, 55, 70, 82].

Recently, fuzzy segmentation algorithm using a modified Mumford-Shah model is proposed by Shen [70] and Thiruvenkadam [77]. Shen [70] and Thiruvenkadam [77] use $0 \le p \le 1$ function instead of a characteristic function u in Equation (3-5). Shen [70] proposed the following minimization problem :

$$\min_{p,c_1,c_2} E(p,c_1,c_2)=\lambda\int_{\Omega}p(I-c_1)^2+(1-p)(I-c_2)^2d\bar{x}+$$

$$\int_{\Omega}(9\epsilon(|\nabla p|^2+|\nabla(1-p)|^2)+\frac{2(p(1-p))^2}{\epsilon})d\bar{x}, \quad (3\text{–}6)$$

where $\epsilon > 0$ and p is a probability measure of image pattern with $0 \le p \le 1$. In [77], $p = cos^2(\theta)$ is presented, where $0 \le \theta \le \frac{\pi}{2}$:

$$\min_{\theta,c_1,c_2} E(\theta,c_1,c_2)=\int_{\Omega}cos^2(\theta)(I-c_1)^2+sin^2(\theta)(I-c_2)^2+\lambda|\nabla\theta|^2+\mu(|\nabla H(\Phi)|)d\bar{x}, \quad (3\text{–}7)$$

where $\phi = cos^2(\theta) - sin^2(\theta)$ and λ and μ are parameters.

In this section, a region based variational partial differential equation model for an image segmentation is presented with an application to synthetic and simulated human brain MRI images. The purpose of the model is to segment borders of the given images. The segmentation is obtained by using a modified Mumford-Shah segmentation technique. The proposed algorithm is motivated by Esedoglu [22], Shen [70], Thiruvenkadam [77], et al.. A fuzzy segmentation in our model is similar to Shen [70] and Thiruvenkadam [77], but the length of boundary term of proposed model is different from Thiruvenkadam [77]. The length of boundary term is motivated by Esedoglu [22], but our model is variational which differs from Esedoglu [22]. Our model is applied to the synthetic image and simulated noisy human brain images. Numerical experiments show the effectiveness of the proposed model to segment given images and the robustness to a noise. This section is organized as follows: In section 3.1.2, a modified Mumford-Shah model is described. Euler-Lagrange equations of the suggested model are presented in this section as well. In section 3.1.3, numerical methods pertaining the proposed model are explained. Experimental results of the model which were applied to synthetic data and simulated human brain MRI images are shown in section 3.1.4.

3.1.2 Description of a Modified Mumford-Shah Model

In this section, a region based segmentation is introduced. The segmentation is attained by using a modified Mumford-Shah segmentation technique. The two phase case is assumed for the simplicity of the problem in our model. The model is aimed to find θ, c_1, and c_2 by minimizing the energy functional:

$$E(\theta, c_1, c_2) = \lambda \int_\Omega (sin^2\theta(\bar{x})(I(\bar{x}) - c_1)^2 + cos^2\theta(\bar{x})(I(\bar{x}) - c_2)^2)d\bar{x} + \int_\Omega (\epsilon sin^2(2\theta(\bar{x}))|\nabla\theta|^2 + \frac{\mu sin^4\theta(\bar{x}) cos^4\theta(\bar{x})}{\epsilon})d\bar{x}, \quad (3\text{-}8)$$

where I is a novel image, Ω is domain, and λ and μ are parameters balancing the influences from the two terms in the model. Here, $0 \leq \theta \leq \pi/2$.

The first term forces $sin^2(\theta(\bar{x}))$, towards 1 if $I(\bar{x})$ is close to c_1 and towards 0 if $I(\bar{x})$ is different from c_1, for every $\bar{x} \in \Omega$. In a similar way, $cos^2(\theta(\bar{x}))$, towards 1 if $I(\bar{x})$ is close to c_2 and towards 0 if $I(\bar{x})$ is different from c_2, for every $\bar{x} \in \Omega$. The second term is the length of boundary term. For every $\bar{x} \in \Omega$, denote $\phi(\bar{x}) = cos^2(\theta(\bar{x})) - sin^2(\theta(\bar{x}))$. If $\phi > 0$, then assign 1 to inside of the given shape c. If $\phi < 0$, then assign 0 to inside of the given shape c. Finally, the segmented binary image is formed.

3.1.2.1 Euler-Lagrange Equations of the Model

The evolution equations associated with the Euler-Lagrange equations in Equation (3-8) are

$$\begin{aligned}\frac{\partial\theta}{\partial t} = -\lambda\{&sin(2\theta(\bar{x}))(I(\bar{x}) - c_1)^2 - sin(2\theta(\bar{x}))(I(\bar{x}) - c_2)^2\} - \\ &\{2\epsilon sin(4\theta(\bar{x}))|\nabla\theta|^2 - 2\epsilon sin^2(2\theta(\bar{x}))\Delta\theta + \\ &\frac{\mu 4 sin^3\theta(\bar{x}) cos^3\theta cos(2\theta(\bar{x}))}{\epsilon}\}, \quad in \ \Omega \\ &\frac{\partial\theta}{\partial n} = 0, \quad on \ \partial\Omega \end{aligned} \tag{3–9}$$

$$\frac{\partial c_1}{\partial t} = -\lambda \int_\Omega sin^2\theta(\bar{x})(I(\bar{x}) - c_1)d\bar{x}, \tag{3–10}$$

$$\frac{\partial c_2}{\partial t} = -\lambda \int_\Omega cos^2\theta(\bar{x})(I(\bar{x}) - c_2)d\bar{x}. \tag{3–11}$$

3.1.3 Numerical Methods

In this section, numerical methods to solve the Equations (3-9)-(3-11) are explained. (3-8) was solved by finding a steady state solution of (3-9)-(3-11). To discretize the equations (3-9)-(3-11), we use a finite difference scheme and we

applied the gradient descent method. Let θ_{ij} denote the value of θ at the pixel $x_i = ih$ and $y_j = jk$, where h and k is the pixel size. Denote $\theta(x_i, y_j, t_n)$ by θ_{ij}^n. The time derivative θ_t at (i, j, t_n) is approximated by the forward difference scheme:

$$\theta_t(i, j, t_n) = \frac{\theta_{ij}^{n+1} - \theta_{ij}^n}{\Delta t},$$

where Δt is the time step. Moreover, (3-2)-(3-4) were implemented by the following iteration scheme :

$$(\theta_x)_{ij}^n = \frac{\theta_{(i+1)j}^n - \theta_{ij}^n}{h},$$

$$(\theta_y)_{ij}^n = \frac{\theta_{i(j+1)}^n - \theta_{ij}^n}{k},$$

$$(\theta_{xx})_{ij}^n = \frac{\theta_{(i+1)j}^n - 2\theta_{ij}^n + \theta_{(i-1)j}^n}{h^2},$$

$$(\theta_{yy})_{ij}^n = \frac{\theta_{i(j+1)}^n - 2\theta_{ij}^n + \theta_{i(j-1)}^n}{k^2}.$$

3.1.4 Experimental Results

The goal of this experiment is to segment the boundary of the object in image using a modified Mumford-Shah technique. Throughout the experiments, $\lambda = 1$ and $\mu = \frac{1}{9}$ are used. The numerical results with an application to the synthetic image are from Figure 3-1 to Figure 3-3. Left image of Figure 3-1 represents a novel image, middle image is $\theta(\bar{x})$, and the right image is $H(\phi(\bar{x})) = 1$, if $\phi(\bar{x}) \geq 0$ and $H(\phi(\bar{x})) = 0$, if $\phi(\bar{x}) < 0$, where $\phi(\bar{x}) = cos^2\theta(\bar{x}) - sin^2\theta(\bar{x})$ and for every $\bar{x} \in \Omega$. In Figure 3-2, left one is the given image and right one is the boundary of the segmented image. Figure 3-3 represents values of c_1 and c_2 in every iteration. Initial value of c_1 is 0.9 and converges to 0.9926 after 80 iterations. In a similar way, c_2 converges to 0.1925 from an initial value 0.5 after 80 iterations.

The results of an application to the simulated human brain MRI images are from Figure 3-4 to Figure 3-9. The data is obtained from `http://www.bic.mni.mcgill.ca/brainweb`. Simulated MRI volumes for normal brain with T1 modality

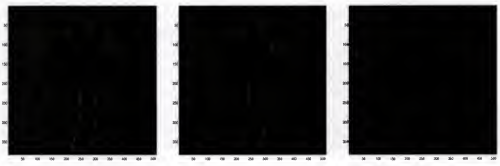

Figure 3–1: Left : A Novel Image, Middle : $\theta(\bar{x}), \bar{x} \in \Omega$, Right : Segmented Image by $H(\phi(\bar{x})), \bar{x} \in \Omega$

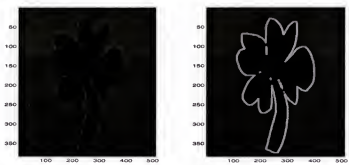

Figure 3–2: Left : A Novel Image, Right : The Boundary of the Segmented Image

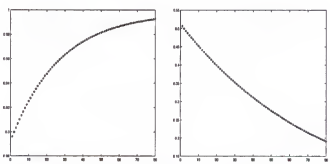

Figure 3–3: Left : c_1 values, Right : c_2 values in each iteration from Figure 3-1

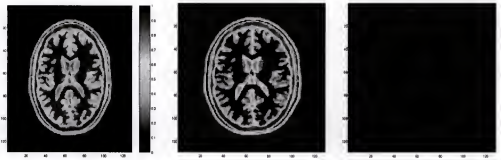

Figure 3-4: Left : A Novel Image, Middle : $\theta(\bar{x}), \bar{x} \in \Omega$, Right : Segmented Image by $H(\phi(\bar{x})), \bar{x} \in \Omega$

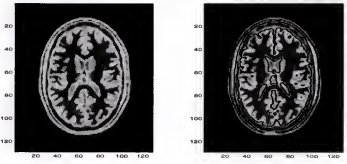

Figure 3-5: Left : A Novel Image, Right : The Boundary of the Segmented Image

are obtained. Slice thickness is $1mm$ with 9% noise and 20% non-uniformity intensity level. Numerical results from our model show From Figure 3-4 to Figure 3-6. The goal is to segment light blue color of the given simulated brain image. Left image of Figure 3-4 represents $\theta(\bar{x})$ values and the right image is $H(\phi(\bar{x})) = 1$, if $\phi(\bar{x}) \geq 0$ and $H(\phi(\bar{x})) = 0$, if $\phi(\bar{x}) < 0$, where $\phi(\bar{x}) = cos^2\theta(\bar{x}) - sin^2\theta(\bar{x})$ and for every $\bar{x} \in \Omega$. The left one is given image and the right one is the boundary of the segmented image in Figure 3-5. Figure 3-6 represents values of c_1 and c_2 in every iteration. Initial value of c_1 is 0.01 which converges to 0.2126 after 80 iterations and c_2 converges to 0.6467 from an initial value 0.4 after 80 iterations.

Another numerical result with an applications to simulated human brain image are shown from Figure 3-7 to Figure 3-9. The goal is to segment light yellow color of the simulated brain image. Left image of Figure 3-7 represents $\theta(\bar{x})$ values and

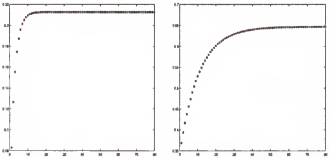

Figure 3-6: Left : c_1 values, Right : c_2 values in each iteration from Figure 3-4

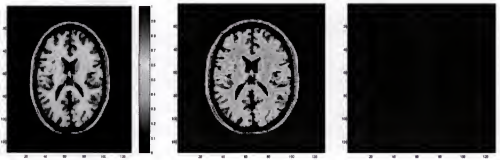

Figure 3-7: Left : A Novel Image, Middle : $\theta(\bar{x}), \bar{x} \in \Omega$, Right : Segmented Image by $H(\phi(\bar{x})), \bar{x} \in \Omega$

the right image is $H(\phi(\bar{x})) = 1$, if $\phi(\bar{x}) \geq 0$ and $H(\phi(\bar{x})) = 0$, if $\phi(\bar{x}) < 0$, where $\phi(\bar{x}) = cos^2\theta(\bar{x}) - sin^2\theta(\bar{x})$ and for every $\bar{x} \in \Omega$. The left one is given image and the right one is the boundary of the segmented image in Figure 3-8. Figure 3-9 represents values of c_1 and c_2 in every iteration. Initial value of c_1 is 0.01 which converges to 0.1110 after 225 iterations and c_2 converges to 0.3474 from an initial value 0.4 after 225 iterations.

3.2 Region Based Segmentation with Shape Prior

3.2.1 Introduction

There have been several algorithms to develop region based segmentation technique using the region statistics or homogeneity presented by Chan, Vese, Mumford, Shah, Zhu, et al. [9, 10, 57, 93]

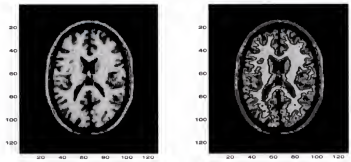

Figure 3–8: Left : A Novel Image, Right : The Boundary of the Segmented Image

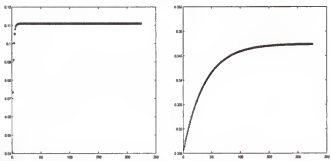

Figure 3–9: Left : c_1 values, Right : c_2 values in each iteration from Figure 3-7

Due to significant signal loss, noise, and non-uniformity of regional intensities, prior information is necessary to make the resulting segmentation more accurate. Cremers, et. al. [19] incorporated statistical shape knowledge into Mumford-Shah segmentation scheme [57] by minimizing a functional that includes both shape energy and the Mumford-Shah energy. A parametric shape model was built proposed by Tsai, et al. [75] and the parameters adjusted to minimize a region based objective function which provides the segmentation. In Chen, Tagare, et al. [15], the shape model was created by averaging the aligned training samples. Better maps were gathered by matching the evolving interface to the shape prior. The geometric active contour was minimized and the shape disparity energy function between the active contour and prior shape was measured by a distance function. Recently, deformable models incorporated by the prior shape and intensity information have been proposed by Metaxas, Huang, et al. [31, 32].

A class of deformable models called MetaMorphs which possess both shape and interior texture statistics integrate boundary and region information coherently in a common variational framework [32]. The MetaMorphs models [32] are extended into a unified shape and intensity space by implicitly representing shapes as images in the space of distance transforms. A novel stochastic chord based matching algorithms align global transformation considering both shape and gray-level intensity information [31]. In the proposed model, it is assumed that the prior shape is close to a novel image which is a similar approach from An, Chen, et al. [2]. But the presented model is designed for the images which have homogenous regions and it is simple to implement.

In this section, a new variational image segmentation model based on the region intensity information using shape knowledge is suggested. The goal of the model is to develop the shape knowledge based segmentation technique. The prior shape information is obtained by using a modified Mumford-Shah segmentation. The prior shape information is supporting the image segmentation process to a given novel image. But prior shape information is formed a binary image in our model. This section is organized as follows: In section 3.2.2, the proposed model is introduced. Euler-Lagrange equations of the suggested model are presented in this section as well. In section 3.2.3, numerical methods pertaining the proposed model are explained. Experimental results of the model which were applied to 2D synthetic data and human brain MRI images are shown in section 3.2.4.

3.2.2 Description of the Proposed Model

A new variational image registration model based on the region intensity information using shape knowledge is suggested. The goal of the model is to develop the prior shape knowledge based image segmentation technique. The prior shape information is obtained by using a modified Mumford-Shah segmentation

technique. The segmentation is assisted by a prior shape binary image and a registration.

Let c be a given shape. A binary image S presents prior shape information which is formed by assigning inside of c to 1 and outside of c to 0. I ia a novel image and Υ is a registration mapping either a rigid transformation or nonrigid deformation. The model is aimed to find Υ, c_1, and c_2 by minimizing the energy functional:

$$E(\Upsilon, c_1, c_2) = \int_\Omega S(\bar{x})(I(\Upsilon(\bar{x})) - c_1)^2 d\bar{x} +$$
$$\lambda \int_\Omega (1 - S(\bar{x}))(I(\Upsilon(\bar{x})) - c_2)^2 d\bar{x} + \nu \int_\Omega |\nabla \Upsilon|^2 d\bar{x}, \tag{3–12}$$

where λ and ν are positive parameters balancing the influences from three terms in the model. For each $\bar{x} \in \Omega$, the first term is forcing $I(\Upsilon(\bar{x}))$ to be close to c_1, since $S(\bar{x}) = 1$ for $\bar{x}$ inside of c. In a similar way, the second term is compelling $I(\Upsilon(\bar{x}))$ to be close to c_2, since $1 - S(\bar{x}) = 1$ for $\bar{x}$ outside of c. Smoothing the vector $\Upsilon(\bar{x})$ is in the last term. After minimizing these three terms, the best Υ, c_1, and c_2 are obtained. In our numerical experiments, only rigid transformations are considered, but the model can be generalized to non-rigid deformation as well. Therefore the rigid transformation vector $\Upsilon(\bar{x}) = \mu R\bar{x} + T$, where μ is a scaling, R is a rotation matrix with respect to an angle θ, and T is a translation. Since the rigid transformation is considered, $\nu = 0$ in our experiments.

3.2.2.1 Euler-Lagrange Equations of the Proposed Model

The evolution equations associated with the Euler-Lagrange equations in Equation (3-12) are

$$\frac{\partial \mu}{\partial t} = \int_\Omega S(\bar{x})(I(\Upsilon(\bar{x})) - c_1)(\nabla I(\Upsilon(\bar{x})))R\bar{x}d\bar{x} +$$
$$\lambda \int_\Omega (1 - S(\bar{x}))(I(\Upsilon(\bar{x})) - c_2)(\nabla I(\Upsilon(\bar{x})))R\bar{x}d\bar{x}, \tag{3–13}$$

$$\frac{\partial \theta}{\partial t} = \int_{\Omega} S(\bar{x})(I(\Upsilon(\bar{x})) - c_1)(\nabla I(\Upsilon(\bar{x})))\mu \frac{dR}{d\theta}\bar{x}d\bar{x} +$$
$$\lambda \int_{\Omega} (1 - S(\bar{x}))(I(\Upsilon(\bar{x})) - c_2)(\nabla I(\Upsilon(\bar{x})))\mu \frac{dR}{d\theta}\bar{x}d\bar{x}, \tag{3-14}$$

$$\frac{\partial T}{\partial t} = \int_{\Omega} S(\bar{x})(I(\Upsilon(\bar{x})) - c_1)(\nabla I(\Upsilon(\bar{x})))d\bar{x} +$$
$$\lambda \int_{\Omega} (1 - S(\bar{x}))(I(\Upsilon(\bar{x})) - c_2)(\nabla I(\Upsilon(\bar{x})))d\bar{x}, \tag{3-15}$$

$$\frac{\partial c_1}{\partial t} = -\int_{\Omega} S(\bar{x})(I(\Upsilon(\bar{x})) - c_1)d\bar{x}, \tag{3-16}$$

$$\frac{\partial c_2}{\partial t} = -\lambda \int_{\Omega} (1 - S(\bar{x}))(I(\Upsilon(\bar{x})) - c_2)d\bar{x}, \tag{3-17}$$

where R is the rotation matrix in terms of the angle θ.

3.2.3 Numerical Methods

In this section, numerical methods to solve the Equations (3-13)-(3-17) are explained. (3-12) was solved by finding a steady state solution of (3-13)-(3-17). To discretize the equations (3-13)-(3-17), we use a finite difference scheme and we applied the gradient descent method. Let $I(\Upsilon)_{ij}$ denote the value of $I(\Upsilon)$ at the pixel $x_i = ih$ and $y_j = jk$, where h and k is the pixel size. Denote $I(\Upsilon)(x_i, y_j, t_n)$ by $I(\Upsilon)^n_{ij}$. The time derivative $I(\Upsilon)_t$ at (i, j, t_n) is approximated by the forward difference scheme:

$$I(\Upsilon)_t(i, j, t_n) = \frac{I(\Upsilon)^{n+1}_{ij} - I(\Upsilon)^n_{ij}}{\Delta t},$$

where Δt is the time step. Moreover, (3-13)-(3-17) were implemented by the following iteration scheme :

$$(I(\Upsilon)_x)^n_{ij} = \frac{I(\Upsilon)^n_{(i+1)j} - I(\Upsilon)^n_{ij}}{h},$$

$$(I(\Upsilon)_y)^n_{ij} = \frac{I(\Upsilon)^n_{i(j+1)} - I(\Upsilon)^n_{ij}}{k}.$$

3.2.4 Experimental Results

The goal of this experiment is to develop the prior shape knowledge based image segmentation technique. The prior shape information is obtained by using a modified Mumford-Shah segmentation technique in section (3.1.2). Throughout experiments, $\lambda = 1$ is used.

The results of an application to the simulated human brain MRI images are from Figure 3-10 to Figure 3-13. The data is obtained from `http://www.bic.mni.mcgill.ca/brainweb`. Simulated MRI volumes for normal brain with T1 modality are obtained. Slice thickness is $1mm$ with 9% noise and 20% non-uniformity intensity level. The goal of the experiment is to segment the light blue color of the simulated brain image. In Figure 3-10, the left one is the simulated MRI brain image BI and the right one is given binary image as feature information S. S is formed by assigning the inside of the given shape c to 1 and outside 0. A novel image I is created by rotating BI by 0.1745. In Figure 3-11, the left one is a novel simulated MRI brain image I and the middle one is segmented image as a binary image. The middle image in Figure 3-11 is created by applying Υ to the prior shape binary image S. Finally, the right one in Figure 3-11 is the boundary of the segmented image. After 90 iterations, θ converges to -0.1763. Initial value of c_1 is 0.1 and converges to 0.1002 after 90 iterations. In a similar way, c_2 converges to 0.4982 from an initial value 0.5 after 90 iterations.

Another numerical results with an applications to simulated human brain image are shown from Figure 3-12 to Figure 3-13. The goal of the experiment is to segment the light yellow color of the simulated brain image. Figure 3-12, the left one is the simulated MRI brain image BI and the right one is given binary image as feature information S. S is formed by assigning the inside of the given shape c to 1 and outside 0. A novel image I is created by rotating BI by -0.2618. In Figure 3-13, the left one is a novel simulated MRI brain image I and the middle one is

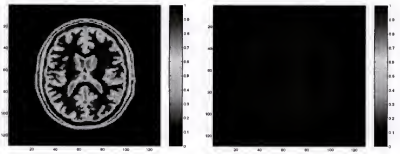

Figure 3–10: Left : Simulated MRI image BI, Right : S

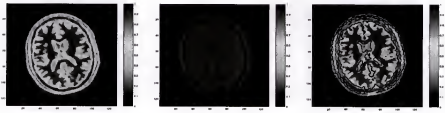

Figure 3–11: Left : A Novel Image I, Middle : Segmented Image, Right : The Boundary of the Segmented Image

segmented image as a binary image. The middle image in Figure 3-13 is created by applying Υ to the prior shape binary image S. Finally, the right one in Figure 3-13 is the boundary of the segmented image. After 155 iterations, θ converges to 0.2531. Initial value of c_1 is 0.09 and converges to 0.0901 after 155 iterations. In a similar way, c_2 converges to 0.0108 from an initial value 0.01 after 155 iterations. The numerical results show the preliminary effectiveness of the proposed model to segment given image using a prior shape binary image.

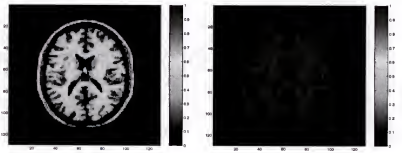

Figure 3–12: Left : Simulated MRI image BI, Right : S

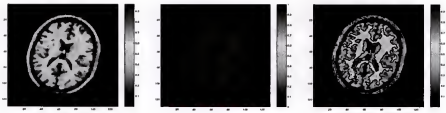

Figure 3–13: Left : A Novel Image I, Middle : Segmented Image, Right : The Boundary of the Segmented Image

3.3 Simultaneous Segmentation and Registration using a Modified Mumford-Shah Model

3.3.1 Introduction

Extracting the boundary and register the given images is one of the most important tasks in image processing, image analysis, and computer vision. There have been numerous techniques developed to solve image segmentation and registration problems. In the past, solutions of these two problems have been studied separately.

Segmentation techniques have been developed to capture the object boundary by several different approaches; edge-based methods mainly using active contour models, region-based methods, or the combination of the two by using Geodesic Active Region models. The most celebrated region based image segmentation model is introduced by Mumford and Shah in 1989 [57]. In this model, an image is decomposed into a set of regions within the bounded open set Ω and these regions are separated by smooth edges Γ. Chan and Vese [9] reformulate a piecewise constant Mumford-Shah model in the context of region based active contour. Chan and Vese also proposed a piecewise constant Mumford-Shah model in [9, 10] by using a level set formulation presented by Osher and Fedkiw [58]. Recently, fuzzy segmentation algorithm using Mumford-Shah model is proposed by Shen [70] and Thiruvenkadam [77]. A fuzzy segmentation in our model is similar to Shen [70] and Thiruvenkadam [77], but the length of boundary term of proposed model is

different from Thiruvenkadam [77]. The length of boundary term is motivated by Esedoglu, et al. [22], but our model is variational which differs from Esedoglu, et al. [22].

Image registration is the process of overlaying two or more images of the same scene taken at different times, and/or by different sensors. Area based methods or feature based methods have been developed to match given images. For the details of the image registration techniques, refer to [92].

A joint segmentation and registration methods have been developed by Chen, Yezzi, Young, et al. [2, 13, 15, 88, 89, 90]. An explicit combination of registration with segmentation has been developed in a variational framework through active contours by Yezzi, Zollei, and Kapur [88, 89]. Moelich and Chan [56] extend the algorithms of Yezzi, Zollei, and Kapur [88] to joint segmentation and of an object in two images, and the prior knowledge is implicitly incorporated through the simultaneous evolution of the registration maps and the active contour in the variational framework. The morphing active contours algorithm is combined with the joint segmentation and registration with an application to CT scans for radiotherapy treatment planning presented by Levy, et al. [90].

The purpose of the model is segment and register given images simultaneously using a modified Mumford-Shah technique and region intensity values. The model performs a simultaneous segmentation and registration in a similar way from Yezzi, et al. [88, 89]. But the model differs from Yezzi, et al. [88, 89] by using a region intensity and a modified Mumford-Shah segmentation technique. This section is organized as follows: In section 3.3.2, the model is proposed for a simultaneous segmentation and registration and the Euler-Lagrange equations of the proposed model is described. In section 3.3.3, numerical methods pertaining to the model are explained. Experimental results of the model which were applied to synthetic

and human brain MRI images are also showed in this section. In section 3.3.4, the conclusion follows and future work is stated.

3.3.2 Description of the Proposed Model

A new variational region based model for a simultaneous image segmentation and registration using a modified Mumford-Shah technique is suggested. The purpose of the model is segment and register given images simultaneously using a modified Mumford-Shah technique and region intensity values. The segmentation is obtained by minimizing a modified Mumford-Shah model. A global rigid registration is assisted by the segmentation information and region intensity value. A segmentation and registration process is obtained simultaneously in this model. The model is aimed to find Θ, c_1, c_2, Υ, d_1, and d_2 by minimizing the energy functional:

$$E(\Theta, c_1, c2, \Upsilon, d_1, d_2) = \lambda_1 \int_\Omega (sin^2\Theta(\bar{x})(I_1 - c_1)^2 + cos^2\Theta(\bar{x})(I_1 - c_2)^2)d\bar{x} +$$

$$\int_\Omega (\epsilon sin^2(2\Theta(\bar{x}))|\nabla\Theta|^2 + \frac{\lambda_2 sin^4\Theta(\bar{x}) cos^4\Theta(\bar{x})}{\epsilon})d\bar{x} + \lambda_3 \int_\Omega |\nabla\Upsilon|^2 d\bar{x}$$

$$\lambda_4 \int_\Omega (sin^2\Theta(\bar{x})(I_2(\Upsilon(\bar{x})) - d_1)^2 + cos^2\Theta(\bar{x})(I_2(\Upsilon(\bar{x})) - d_2)^2)d\bar{x} \qquad (3\text{-}18)$$

where I_1 and I_2 are novel images, Ω is domain, and $\lambda_i > 0$ $(i = 1, 2, 3, 4)$ are parameters balancing the influences from the four terms in the model.

The first term forces $sin^2(\Theta(\bar{x}))$, towards 0 if $I_1(\bar{x})$ is different from c_1 and towards 1 if $I_1(\bar{x})$ is close to c_1, for every $\bar{x} \in \Omega$. For $\bar{x} \in \Omega$, the average intensity of $I_1(\bar{x})$ is close to c_1, where $sin^2(\Theta(\bar{x})) > cos^2(\Theta(\bar{x}))$. In a similar way, $cos^2(\Theta(\bar{x}))$, towards 0 if $I_1(\bar{x})$ is different from c_2 and towards 1 if $I_1(\bar{x})$ is close to c_2, for every $\bar{x} \in \Omega$. For $\bar{x} \in \Omega$, the average intensity of $I_1(\bar{x})$ is close to c_2, where $sin^2(\Theta(\bar{x})) < cos^2(\Theta(\bar{x}))$. The second term is a length of boundary term. Smoothing the vector $\Upsilon(\bar{x})$ is in the third term. For each $\bar{x} \in \Omega$, the fourth term is forcing $sin^2(\Theta(\bar{x}))$, towards 0 if $I_2(\Upsilon(\bar{x}))$ is different from d_1 and towards 1 if $I_2(\Upsilon(\bar{x}))$ is close to d_1.

For $\bar{x} \in \Omega$, the average intensity of $I_2(\Upsilon(\bar{x}))$ is close to d_1, where $sin^2(\Theta(\bar{x})) > cos^2(\Theta(\bar{x}))$. In a similar way, $cos^2(\Theta(\bar{x}))$, towards 0 if $I_2(\Upsilon(\bar{x}))$ is different from d_2 and towards 1 if $I_2(\Upsilon(\bar{x}))$ is close to d_2. For $\bar{x} \in \Omega$, the average intensity of $I_2(\Upsilon(\bar{x}))$ is close to d_2, where $sin^2(\Theta(\bar{x})) < cos^2(\Theta(\bar{x}))$. After minimizing these three terms, the best Θ, Υ, c_1, c_2, d_1, and d_2 are obtained. For every $\bar{x} \in \Omega$, denote $\phi(\bar{x}) = sin^2(\Theta(\bar{x})) - cos^2(\Theta(\bar{x}))$. If $\phi > 0$, then assign 1 to inside of the given shape c. If $\phi < 0$, then assign 0 to inside of the given shape c. The segmented binary image of I_1 is formed. In a similar way, $H(\phi(\Upsilon))$ segments a novel image I_2 by forming a binary image which has a 1 inside of the given shape d and 0 outside of d.

In our numerical experiments, only rigid transformation is considered, but the model can be generalized to non-rigid deformation as well. Therefore the rigid transformation vector $\Upsilon(\bar{x}) = \mu R\bar{x} + T$, where μ is a scaling, R is a rotation matrix with respect to an angle θ, and T is a translation. Since the rigid transformation is considered, $\lambda_3 = 0$ in our experiments.

3.3.2.1 Euler-Lagrange Equations of the Proposed Model

The evolution equations associated with the Euler-Lagrange equations in Equation (3-18) are

$$\begin{aligned}\frac{\partial\Theta}{\partial t} = {} & \lambda_1(sin(2\Theta(\bar{x}))(I_1 - c_1)^2 - sin(2\Theta(\bar{x}))(I_1 - c_2)^2)d\bar{x} \\ & -\{2\epsilon sin(4\Theta(\bar{x}))|\nabla\Theta|^2 - 2\epsilon sin^2(2\Theta(\bar{x}))\Delta\Theta \\ & +\frac{\lambda_2 4 sin^3\Theta(\bar{x}) cos^3\Theta(\bar{x}) cos(2\Theta(\bar{x}))}{\epsilon})d\bar{x} \\ & +\lambda_1(sin(2\Theta(\bar{x}))(I_2 - d_1)^2 - sin(2\Theta(\bar{x}))(I_2 - d_2)^2)d\bar{x}, \quad in\ \Omega \\ & \frac{\partial\Theta}{\partial n} = 0, \quad on\ \partial\Omega \end{aligned} \tag{3-19}$$

$$\frac{\partial c_1}{\partial t} = -\lambda_1 \int_\Omega sin^2\Theta(\bar{x})(I_1(\Upsilon(\bar{x})) - c_1)d\bar{x}, \tag{3-20}$$

$$\frac{\partial c_2}{\partial t} = -\lambda_1 \int_\Omega cos^2\Theta(\bar{x})(I_1(\Upsilon(\bar{x})) - c_2)d\bar{x}. \tag{3-21}$$

$$\begin{aligned}\frac{\partial \mu}{\partial t} = \lambda_4 \int_\Omega (sin(2\Theta(\bar{x}))(I_2(\Upsilon(\bar{x}))) - d_1)^2 - sin(2\Theta(\bar{x})) \\ (I_2(\Upsilon(\bar{x}))) - d_2)^2)R\bar{x}d\bar{x} + \lambda_4 \int_\Omega sin^2\Theta(\bar{x}) \\ (I_2(\Upsilon(\bar{x})) - d_1)(\nabla I_2(\Upsilon(\bar{x})))R\bar{x} + \\ cos^2\Theta(\bar{x})(I_2(\Upsilon(\bar{x})) - d_2)(\nabla I_2(\Upsilon(\bar{x})))R\bar{x}d\bar{x},\end{aligned} \tag{3-22}$$

$$\begin{aligned}\frac{\partial \theta}{\partial t} = \lambda_4 \int_\Omega (sin(2\Theta(\bar{x}))(I_2(\Upsilon(\bar{x}))) - d_1)^2 - sin(2\Theta(\bar{x})) \\ (I_2(\Upsilon(\bar{x}))) - d_2)^2)\mu\frac{dR}{d\theta}\bar{x}d\bar{x} + \lambda_4 \int_\Omega sin^2\Theta(\bar{x}) \\ (I_2(\Upsilon(\bar{x})) - d_1)(\nabla I_2(\Upsilon(\bar{x})))\mu\frac{dR}{d\theta}\bar{x} + \\ cos^2\Theta(\bar{x})(I_2(\Upsilon(\bar{x})) - d_2)(\nabla I_2(\Upsilon(\bar{x})))\mu\frac{dR}{d\theta}\bar{x}d\bar{x},\end{aligned} \tag{3-23}$$

$$\begin{aligned}\frac{\partial T}{\partial t} = \lambda_4 \int_\Omega (sin(2\Theta(\bar{x}))(I_2(\Upsilon(\bar{x}))) - d_1)^2 - sin(2\Theta(\bar{x})) \\ (I_2(\Upsilon(\bar{x}))) - d_2)^2)d\bar{x} + \lambda_4 \int_\Omega sin^2\Theta(\bar{x}) \\ (I_2(\Upsilon(\bar{x})) - d_1)(\nabla I_2(\Upsilon(\bar{x})))+ \\ cos^2\Theta(\bar{x})(I_2(\Upsilon(\bar{x})) - d_2)(\nabla I_2(\Upsilon(\bar{x})))d\bar{x},\end{aligned} \tag{3-24}$$

$$\frac{\partial d_1}{\partial t} = -\lambda_4 \int_\Omega sin^2\Theta(\bar{x})(I_2(\Upsilon(\bar{x})) - d_1)d\bar{x}, \tag{3-25}$$

$$\frac{\partial d_2}{\partial t} = -\lambda_4 \int_\Omega cos^2\Theta(\bar{x})(I_2(\Upsilon(\bar{x})) - d_2)d\bar{x}, \tag{3-26}$$

where R is the rotation matrix in terms of the angle θ.

3.3.3 Numerical Methods

In this section, numerical methods to solve the Equations (3-19)-(3-26) are explained. (3-18) was solved by finding a steady state solution of (3-19)-(3-26). To discretize the equations (3-19)-(3-26), we use a finite difference scheme and we applied the gradient descent method. Let Θ_{ij} denote the value of Θ at the pixel $x_i = ih$ and $y_j = jk$, where h and k is the pixel size. Denote $\theta(x_i, y_j, t_n)$ by Θ^n_{ij}. The time derivative Θ_t at (i, j, t_n) is approximated by the forward difference scheme:

$$\Theta_t(i, j, t_n) = \frac{\Theta^{n+1}_{ij} - \Theta^n_{ij}}{\Delta t},$$

where Δt is the time step. $I(\Upsilon)_{ij}$ denote the value of $I(\Upsilon)$ at the pixel $x_i = ih$ and $y_j = jk$, where h and k is the pixel size. Denote $I_2(\Upsilon)(x_i, y_j, t_n)$ by $I_2(\Upsilon)^n_{ij}$. The time derivative $I_2(\Upsilon)_t$ at (i, j, t_n) is approximated by the forward difference scheme:

$$I_2(\Upsilon)_t(i, j, t_n) = \frac{I_2(\Upsilon)^{n+1}_{ij} - I_2(\Upsilon)^n_{ij}}{\Delta t},$$

where Δt is the time step. Moreover, (3-19)-(3-26) were implemented by the following iteration scheme :

$$(\Theta_x)^n_{ij} = \frac{\Theta^n_{(i+1)j} - \Theta^n_{ij}}{h},$$

$$(\Theta_y)^n_{ij} = \frac{\Theta^n_{i(j+1)} - \Theta^n_{ij}}{k},$$

$$(\Theta_{xx})^n_{ij} = \frac{\Theta^n_{(i+1)j} - 2\Theta^n_{ij} + \Theta^n_{(i-1)j}}{h^2},$$

$$(\Theta_{yy})^n_{ij} = \frac{\Theta^n_{i(j+1)} - 2\Theta^n_{ij} + \Theta^n_{i(j-1)}}{k^2}.$$

$$(I_2(\Upsilon)_x)^n_{ij} = \frac{I_2(\Upsilon)^n_{(i+1)j} - I_2(\Upsilon)^n_{ij}}{h},$$

$$(I_2(\Upsilon)_y)^n_{ij} = \frac{I_2(\Upsilon)^n_{i(j+1)} - I_2(\Upsilon)^n_{ij}}{k}.$$

3.3.4 Experimental Results

The purpose of this experiment is segment and register given images simultaneously using a modified Mumford-Shah technique and region intensity values. The segmentation is obtained by minimizing a modified Mumford-Shah model. Throughout the experiments, $\lambda_1 = 3$, $\lambda_2 = 1/9$, and $\lambda_4 = 1$ are used. The results of an application to the simulated human brain MRI images are from Figure 3-14 to Figure 3-17. The data is obtained

from *http://www.bic.mni.mcgill.ca/brainweb*. Simulated MRI volumes for normal brain with T1 modality are obtained. Slice thickness is $1mm$ with 9% noise and 20% non-uniformity intensity level. For Figure 3-14 and Figure 3-15, a given image I_2 is created by rotating an image I_1, by amount of 0.1745. In Figure 3-14, from left to right, the first one is a novel image I_1, the second one is a novel image I_2, and the third one is a segmented image of I_1. For every $\bar{x} \in \Omega$, denote $\phi(\bar{x}) = sin^2(\Theta(\bar{x})) - cos^2(\Theta(\bar{x}))$. If $\phi > 0$, then assign 1 to inside of the given shape c. If $\phi < 0$, then assign 0 to inside of the given shape c. The segmented binary image of I_1 is formed by $H(\phi(\bar{x}))$. In Figure 3-15, from left to right, the first one is the boundary of the segmented image of I_1. The second one is segmented binary image of I_2 formed by $H(\phi(\Upsilon))$. Finally, the third one is the boundary of the segmented image of I_2. After 20 iterations, θ converges to -0.1776. Initial value of c_1 is 0.01 which converges to 0.1173 after 20 iterations and c_2 converges to 0.5907 from an initial value 0.04 after 20 iterations. In a similar way, initial value of d_1 is 0.02 which converges to 0.1404 after 20 iterations and d_2 converges to 0.5393 from an initial value 0.05 after 20 iterations.

Finally, a given image I_2 is created by rotating an image I_1, by amount of -0.2618 for Figure 3-16 and Figure 3-17. In Figure 3-16, from left to right, the first one is a novel image I_1, the second one is a novel image I_2, and the third one is a segmented image of I_1. For every $\bar{x} \in \Omega$, denote $\phi(\bar{x}) = sin^2(\Theta(\bar{x})) - cos^2(\Theta(\bar{x}))$. If

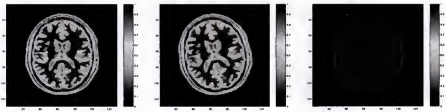

Figure 3–14: Left : A Novel Image I_1, Middle : A Novel Image I_2, Right : Segmented Image of I_1

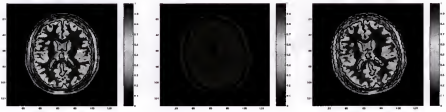

Figure 3–15: Left : The Boundary of the Segmented Image I_1, Middle : Segmented Image of I_2, Right : The Boundary of the Segmented Image of I_2

$\phi > 0$, then assign 1 to inside of the given shape c. If $\phi < 0$, then assign 0 to inside of the given shape c. The segmented binary image of I_1 is formed by $H(\phi(\bar{x}))$. In Figure 3-17, from left to right, the first one is the boundary of the segmented image of I_1. The second one is segmented binary image of I_2 formed by $H(\phi(\Upsilon))$. Finally, the third one is the boundary of the segmented image of I_2. After 20 iterations, θ converges to 0.2568. Initial value of c_1 is 0.45 which converges to 0.4496 after 20 iterations and c_2 converges to 0.0293 from an initial value 0.2 after 20 iterations. In a similar way, initial value of d_1 is 0.55 which converges to 0.4263 after 20 iterations and d_2 converges to 0.0548 from an initial value 0.4 after 20 iterations. The experimental results show the effectiveness of the model in detecting the boundaries of the given objects and registering novel images simultaneously and robustness to a noise.

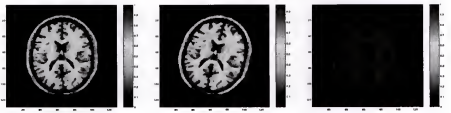

Figure 3–16: Left : A Novel Image I_1, Middle : A Novel Image I_2, Right : Segmented Image of I_1

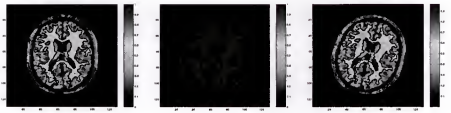

Figure 3–17: Left : The Boundary of the Segmented Image of I_1, Middle : Segmented Image of I_2, Right : The Boundary of the Segmented Image of I_2

CHAPTER 4
CONCLUSIONS AND FUTURE DIRECTION

In Chapter 2, a new variational method for a simultaneous segmentation and non-rigid registration that incorporates the shape and intensity priors is proposed. Since the heart cardiac images can be varied images to images, a local non-rigid deformation term is added to capture the boundary effectively. Numerical results showed the effectiveness of the suggested model.

The prior shape C^* and prior image I^* which were created by using the method from [12] are in Figure 2-1. The average contour is used as a prior shape and an average image for a prior intensity. From Figure 2-2 to Figure 2-3, the effectiveness of each term in the model. From Table 2-1, it is easily seen that the major contribution terms in the model are the first and third terms. From Figure 2-4 to Figure 2-7, the model performance to the given images which is compared to expert borders is shown. The global rigid transformation model was calculated in Equation (2.9) without $\begin{bmatrix} u \\ v \end{bmatrix}$ term. The distance measurements of the results of the model from the expert's borders by using the distance function are followed in Table 2-2 and Table 2-3. The results show the effectiveness of the model to capture the boundary of the given image, which is better than the model with global rigid transformation term only. These results were obtained through Matlab and the computational time in each iteration was about 1 second using a Pentium 4 CPU running at 2.4 GHZ with 512 MB of RAM. Windows XP Home Edition was used as the operating system.

Due to the inhomogeneity, dropout, and loss of some information near the edges in heart images, parameters are adjusted in each image to get desired results.

Some of the images with a diminishing problem which depends on the parameters are observed in the experiments. Since the shape prior is used as an initial contour, the level set form of the model is fixed which does not require the re-initialization process during the numerical calculation. The intensity matching term in the energy function of the model provides the difference of the intensity variation across the prior shape and the shape of interest. Minimizing the difference of the gradients of the intensity between smoothed prior image and the smoothed given image is more accurate than minimizing the gradient term in the given image, due to the loss of the information of the gradient near the edge of the desired object. Moreover, this model can be extended to 3D cases and any other types of images. Generalization of the model to global non-rigid deformation is needed in future work.

Several statistical algorithms for generating shape models are presented. The aim of the models is to develop an approach for the mean shape and clustering to detect differences in the shape of anatomical structures. One of the suggested models minimizes a shape related energy to create the mean shape with the orthogonal Procrustes method. The model does not depend upon the choice of the initial contour and generates the mean shape and alignments to the mean shape from the given contours simultaneously. The other models generate the mean shape and clustering by using Self-Organizing map. The closeness is measured by the orthogonal Procrustes method or area difference distance. This technique has the advantage of generating the mean shape of each cluster and clustering given contours simultaneously. In addition, Self-Organizing map combined with a Principal Component Analysis (PCA) model is also introduced. Numerical results with an application to human-heart normal two-chamber end-diastolic epicardial borders are shown the effectiveness of the suggested models. Figure 2-8 represents the shape related energy function model result applied eighty-five human-heart

end-diastolic epicardial borders. For Figure 2-8, a dotted line in the left one is the initial contour of the given contours. The dotted line in the right one is mean shape of the given contours. Three distance measurements, namely mean distance, standard deviation, and Tanimoto measurement of the result of the models from Figure 2-8 is in Table 2-6. From Figure 2-9 to Figure 2-13 are the results which were obtained when the Self-Organizing map was applied to the eighty-five human-heart two-chamber normal end-diastolic epicardiac borders to obtain clustering and the mean shape of each cluster. Figure 2-9 is the numerical results using Self-Organizing map with the area difference distance method. In a similar way, Figure 2-10 is the numerical results using Self-Organizing map with orthogonal Procrustes method. It is easily seen that the orthogonal method is more efficient than area difference method from Table 2-7. To get better mean shape, Figure 2-11 shows the numerical results using the method from section 2.8.2.3. Pre-alignments and applying principal component analysis give better results which can be easily seen in Table 2-7. From Figure 2-12 and Figure 2-13, numerical results with an application to the eighty-five human-heart two-chamber normal end-diastolic epicardiac borders to cluster into three groups. Figure 2-12 shows the results using the method from section 2.8.2.2 with orthogonal Procrustes method. First group, there are 30 contours, 28 contours are in the second group. Finally 27 contours are in the third group. Numerical results using the method from section 2.8.2.3 is in Figure 2-13. Distance measurements comparisons from Table 2-8 and Table 2-9 show the effectiveness of the suggested models.

Chapter 3 contains three interrelated sections; Image segmentation using a modified Mumford-Shah technique, Region based image segmentation with prior shape, and a modified Mumford-Shah model based simultaneous segmentation and registration.

A region based variational partial differential equation (PDE) model for an image segmentation is presented with an application to synthetic and human brain MRI images. The purpose of the model is to segment borders of the given images. The segmentation is obtained by using a modified Mumford-Shah segmentation technique. The numerical results with an application to the synthetic image and simulated normal human brain images are shown from Figure 3-1 to Figure 3-9. Preliminary numerical results show the effectiveness of the model to capture the boundary of the given fuzzy images.

A new variational region based image segmentation model based on the region intensity and prior shape information is suggested. The prior shape information is extracted by using a modified Mumford-Shah segmentation. The shape knowledge information and registration are supporting the image segmentation process. The model results with an application to simulated human brain images are shown from Figure 3-10 to Figure 3-13. These numerical results show the effectiveness of the suggested model to register given wrongly mapped images correctly. Even though numerical experiments are done only for the global rigid transformation, it can be generalized to global non-rigid deformation. Generalization of the model to global non-rigid deformation is needed for future work.

A new variational region based model for a simultaneous image segmentation and registration using a modified Mumford-Shah technique is presented. The purpose of the model is segment and register given images simultaneously using a modified Mumford-Shah technique and region intensity values. The model results with an application to simulated human brain images are shown from Figure 3-14 to Figure 3-17. The numerical results show the effectiveness of the model in detecting the boundaries of the given objects and registering novel images simultaneously. This model can be extended to 3D cases and any other types of images.

REFERENCES

[1] L. Ambrosio and V. Tortorelli, "Approximation of functionals depending on jumps by elliptic functionals via Γ-convergence," *Comm. on Pure and Applied Math.* vol. 43, pp. 999–1036, 1990.

[2] J. An, Y. Chen, F. Huang, D. Wilson, and E. Geiser, "A variational PDE based level set method for a simultaneous segmentation and non-rigid registration", *Proc.8th. Ann. Int. Conf. on Med. Image Comp. Computer-Assi. Interv. MICCAI*, pp. 286–293, 2005.

[3] S. Baldo, "Minimal interface criterion for phase transitions in mixtures of Cahn-Hilliard fluids," *Annals. Inst. Henri Poincare*, vol. 7, pp. 67–90, 1990.

[4] F. Bookstein, "Size and shape spaces for landmark data in two dimensions," *Statist. Sci.*, vol. 1, pp. 181–242, 1986.

[5] M. Bro-Nielsen and C. Gramkow. "Fast fluid registration of medical images," *Proceedings of Vis. Biomed. Comp.*, pp. 267–276, 1996.

[6] T. Carne, "The geometry of shape spaces," *Proceedings of the London Math. Soc.*, vol. 3, no. 61, pp. 407–432, 1990.

[7] V. Caselles, F. Catté, T. Coll, and F. Dibos, "A geometric model for active contours in image processing," *Numerische Mathematik*, vol. 66, pp. 1–31, 1993.

[8] V. Caselles, R. Kimmel, and G. Sapiro, "On geodesic active contours," *Int. J. Comp. Vis.*, vol. 22, no. 1, pp. 61–79, 1997.

[9] T. Chan and L. Vese, "Active contours without edges," *IEEE Trans. Image Proc.*, 10, 2, pp.266–277, 2001.

[10] T. Chan and L. Vese, "A level set algorithm for minimizing the Mumford-Shah functional in image processing," *Proceedings 1st IEEE Workshop Varia. Level Set Meth. Comp. Vis.*, 13, pp. 161–168, 2001.

[11] C. Chefd'Hotel, G. Hermosillo, and O. Faugeras, "Variational methods for multimodal image matching," *Int. J. Comp. Vis.*, vol. 50, no. 3, pp. 329–343, 2002.

[12] Y. Chen, F. Huang, H. Tagare, M. Rao, D. Wilson, and E. Geiser, "Using prior shapes and intensity profiles in medical image segmentation," *Proceedings of Int. Conf. Comp. Vis.*, pp. 1117–1124, 2003.

[13] Y. Chen, F. Huang, D. Wilson, and E. Geiser, "Segmentation with shape and intensity priors," *Proceedings of Sec. Int. Conf. Image Graph*, pp. 378–385, 2003.

[14] Y. Chen, W. Guo, F. Huang, D. Wilson, and E. Geiser, "Using prior shapes and points in medical image segmentation," *Proceedings of Ener. Mini. Meth. Comp. Vis. Pat. Recog.*, pp.291–305, 2003.

[15] Y. Chen, H. Tagare, S. Thiruvenkadam, F. Huang, D. Wilson, K. Gopinath, R. Briggs, and E. Geiser, "Using prior shapes in geometric active contours in a variational framework," *Int. J. Comp. Vis.*, vol. 50, no. 3, pp. 315–328, 2002.

[16] Y. Chen, D. Wilson, and F. Huang, "A new procrustes methods for generating geometric models," *Proceedings of World Multi. on Syst. Cyber. and Infor.*, pp. 227–232, 2001.

[17] T. Cootes and C. Taylor, "Mixture model for representing shape variation," *Image and Vision Computing*, 17, 8, pp.567–574, 1999.

[18] T. Cootes, C. Taylor, D. Cooper, and J. Graham, "Active shape model - their training and application," *Comp. Vis. and Image Understanding.*, vol. 61, pp. 38–59, 1995

[19] D. Cremers, F. Tischhäuser, J. Weickert, and C. Schnörr, "Diffusion-snakes: Introducing statistical shape knowledge into the Mumford-Shah functional," *Int. J. Comp. Vis.*, vol. 50, no. 3, pp. 295–315, 2002.

[20] I. Dryden and K. Mardia, *Statistical Shape Analysis*, John Wiley & Sons, New York, 1998.

[21] S. Esedoglu and J. Shen, "Digital inpainting based on the Mumford-Shah-Euler image model," *European J. Appl. Math.*, vol. 13, pp. 353–370, 2002.

[22] S. Esedoglu and R. Tsai, "Threshold dynamics for the piecewise constant Mumford-Shah fuctional," *CAM Report 04-63 UCLA*, 2004.

[23] M. Fréchet, "Les courbes aléatoires," *Bull. Inst. Internat. Statist.*, vol. 38, pp. 499–504, 1961.

[24] T. Gaens, F. Maes, D. Vandermeulen, and P. Suetens, "Non-rigid multimodal image registration using mutual information," *Proceedings of First Int. Conf. Med. Image Comp. Computer-Assi. Interv.*, vol. 1496, pp. 1099–1106, 1998.

[25] J. Gee, M. Reivich, and R. Bajcsy, "Elastically deforming 3D atlas to match anatomical brain images," *J. Comp. Assi. Tom.*, vol. 17, no. 2, pp. 225–236, 1993.

[26] F. Gibou and R. Fedkiw, "A fast hybrid k-means level set algorithm for segmenttion," *Stanford Technical Report*, 2002.

[27] N. Hata, "Rigid and deformation medical image registration for image guided surgery," Ph.D Thesis Univ. Tyoko, 1998.

[28] G. Hermosillo, C. Chefd'Hotel, and O. Faugeras, "A variational methods for multimodal image matching," *Int. J. Comp. Vis.*, vol. 50, 3, pp. 329–345, 2002.

[29] P. Hellier and C. Barillot, "Multimodal non-rigid warping for correction of distortions in functional MRI," *Proceedings of Third Int. Conf. Med. Image Comp. Computer-Assi. Interv.*, vol. 1935, pp. 512–520, 2000.

[30] T. Honkela, "Description of Kohonen's Self-Organizing map," *http://www.mlab.uiah.fi/ timo/som/thesis-som.html*, Dec. 6th. 2005.

[31] X. Huang, Z. Li, and D. Metaxas, "Learning coupled prior shape and appearance models for segmentation," *Proc. 7th. Ann. Int. Conf. on Med. Image Comp. Computer-Assi. Interv.*, vol. I LNCS-3216, pp. 60-69, 2004.

[32] X. Huang, D. Metaxas, and T. Chen, "MetaMorphs: deformable shape and texture models," *Proceedings of IEEE Comp. Soc. Conf. Comp. Vis. Pat. Recog.*, vol. I, pp. 496–503, 2004.

[33] M. Kass, A. Witkin, and D. Terzopoulos, "Snakes: active contour models," *Int. J. Comp. Vis.*, no. 1, pp. 321–331, 1987.

[34] D. Kendall, *Stochastic geometry*, John Wiley & Sons, New York, pp. 322–376, 1973.

[35] D. Kendall, "Shape-manifolds, Procrustean metrics, and complex projective spaces," *Bull. London Mathematical Society*, pp. 81–121, 1984.

[36] D. Kendall, "A survey of the statistical theory of shape," *Statist. Sci.*, vol. 4, no. 2, pp. 87–120, 1989.

[37] J. Kent and K. Mardia, "Shape, Procrustes tangent projections and bilateral symmetry," *Biometrika*, 88, pp. 469–485, 2001.

[38] S. Kichenassamy, A. Kumar, P. Olver, A. Tannenbaum, and A. Yezzi, "Gradient flows and geometric active contour models," *Proceedings of ICCV'95*, pp. 810–815, 1995.

[39] K. Koch, *Parameter estimation and hypothesis testing in linear models*, Springer-Verlag, New York, 1987.

[40] T. Kohonen, *Self-Organizing maps*, Springer-Verlag, New York, 2001.

[41] M. Leventon, O. Faugeras, E. Grimson, and W. Wells, "Level set based segmentation with intensity and curvature priors," *Math. Meth. Biomed. Image Anal.*, 2000.

[42] M. Leventon, E. Grimson, and O. Faugeras, "Statistical shape influence in geodesic active contours," *Proceedings of IEEE Conf. CVPR*, pp. 316–323, 2000.

[43] J. Lie, M. Lysaker, and X. Tai, "A binary level set model and some aplications to Mumford-Shah segmentation," *CAM Report*, vol. 31, 2004.

[44] B. Likar and F. Permus, "A hierarchical approach to elastic registration based on mutual information," *Image Vis. Comp.*, 19, (1-2), pp. 33–44. 2000.

[45] J. MacQueen, "Some methods for classification and analysis of multivariate observations," *Proceedings of the Fifth Berkeley Symposium on Mathematical Statistics and Probability*, vol. 1, pp. 281–297, 1967.

[46] F. Maes, A. Collignon, D. Vandermeulen, G. Marchal, and P. Suetens, "Multimodality image registration byn maximization of mutual information," *IEEE Trans. Med. Imaging*, 16, 2, pp.187–198, 1997.

[47] R. Malladi, J. Sethian, and B. Vemuri, "Shape modeling with front propagation: A level set approach," *IEEE Trans. Pat. Anal. machine Intell.*, vol. 17, pp. 158–175, 1995.

[48] S. Mallat, *A wavelet tour of signal processing*. Academy Press, 1998

[49] R. March, "Visual reconstruction with discontinuties using variational methods," *Image Vision and Comput.*, vol. 10. pp. 30–38, 1992.

[50] J. Marroquin, A. Santana, and S. Botello "Hidden markov measure field models for image segmentation," *IEEE trans. on Pattern Anal. Mchine Inte.*, vol. 25, pp. 1380–1387, 2003.

[51] S. Marsland and C. Twining, "Constructing data-driven optimal representations for iterative pairwise non-rigid represenataions," *Proceedings Second Int. Workshop Biomed. Image Reg.*, vol. 2717, pp. 50–60, 2003.

[52] G. Matheron, *Random sets and integral geometry*, John Wiley & Sons, New York, 1975

[53] A. Matheny and D. Goldgof, "Use of three and four dimensional surface harmonics for rigid and non-rigid shape recovery and representation," *IEEE trans. on Pattern Anal. Mchine Inte.*, vol. 17, pp. 967–981, 1995.

[54] C. Meyer, J. Boes, B. Kim, and P. Bland, "Probabilistic brain atlas construction: thin-plate spline warping via maximization of mutual information," *Proc. Second Int. Conf. Med. Image Comp. Computer-Assi. Interv.*, vol. 1679, pp. 631–637, 1999.

[55] L. Modica, "The gradient theory of phase transitions and the minimal interface criterion," *Arch. Rational Mech. Anal.*, Vol. 98, pp. 123–142, 1987.

[56] M. Moelich and T. Chan, "Joint segmentation and registration using logic models," *UCLA CAM Report*, 03-06, 2003.

[57] D. Mumford and J. Shah, "Optimal approximation by piecewise smooth functions and associated variational problems," *Comm. Pure Appl. Math.*, vol. 42, pp. 557–685, 1989

[58] S. Osher and R. Fedkiw, *Level set methods and dynamic implicit surfaces*, Springer-Verlag, New York, 2003.

[59] S. Osher and J. Sethian, "Fronts propagating with curvature-dependent speed: algorithms based on Hamilton-Jacobi formulation," *J. Comp. Phys.*, vol. 79, pp. 12–49, 1988.

[60] N. Paragios, *Geodesic active regions and level set methjods: contributions and applications in artificial vision*, Ph.D. Thesis Sch. Comp. Engin. Uni. Nice/Sophia Antipolis, 2000.

[61] N. Paragios, "A variational approach for the segmentation of the left ventricle in MR cardiac images," *Proceedings of 1st. IEEE Workshop Var. Level Set Met. Comp. Vis.*, pp. 153–160, 2001.

[62] N. Paragios and R. Deriche, "Geodesic active regions for supervised texture segmentation," *IEEE ICCV*, pp. 926–932, 1999.

[63] N. Paragios and M. Rousson, "Shape prior for level set representations," *Comp. Vis.-ECCV2002. the 7th Europ. Conf. on Comp. Vis.*, 2002.

[64] N. Paragios, M. Rousson, and V. Ramesh, "Marching distance functions: a shape-to-area variational approach for global-to-local registration.," *Comp. Vis.-ECCV*, pp. 775–789, 2002.

[65] N. Paragios, M. Rousson, and V. Ramesh, "Knowledge-based registration & segmentation of the left ventricle: A level set approach," *WACV*, pp. 37–42, 2002.

[66] P. Perona and J. Malik, "Scale-space and edger detection using anisotropic diffusion," *IEEE PAMI*, vol. 12, pp. 629–639, 1990.

[67] F. Richard and L. Cohen, "A New Image Registraton Technique with Free Boundary Constraints: Application to Mammography," *ECCV LNCS*, 2353, pp. 531–545, 2002.

[68] D. Rueckert, M. Clarkson, D. Hill, and D. Hawkes, "Non-rigid registration using higher-order mutual information," *Med. Imaging SPIE Proc.*, vol. 3979, pp. 438–447, 2000.

[69] D. Rueckert, L. Sonoda, C. Hayes, D. Hill, M. Leach, and D. Hawkes, "Non-rigid registration using free-form deformations: Application to breast MR images," *IEEE Trans. Med. Imaging*, vol. 18, no. 8, pp. 712–721, 1999.

[70] J. Shen, "A stochastic-variational model for soft Mumford-Shah segmentation," *IMA Preprint series*, vol. 2062, 2005.

[71] S. Soatto and A. Yezzi, "Deformation: deforming motion, shape average and joint registration and segmentation of images," *Comp. Vis. ECCV*, 2002.

[72] B. Song and T. Chan, "A fast algorithm for level set based optimization," *UCLA CAM Report*, 2002.

[73] M. Stegmann and D. Gomez, "A brief introduction to statistical shape anlaysis," *Informa. and Math. Modelling. Technical University of Denmark*, 2002.

[74] S. Suri, "Two-Dimensional fast magnetic resonance brain segmentation," *IEEE Eng. in Medicine and Biology*, vol. 20 no. 4, pp. 84–95, 2001.

[75] A. Tsai, A. Yezzi, and A. Willsky, "Curve evolution implementation of the Mumford-Shah functional for image segmentation, denoising, interpolation, and magnification," *IEEE Trans. Image Proc.*, 10, 8, pp. 1169–1186, 2001.

[76] D. Thompson, *On Growth and Form*, Cambridge Univ. Press, 1917.

[77] S. Thiruvenkadam, *Partial differential equations and variational methods applied to medical image analysis*, Thesis. University of Florida, 2005.

[78] B. Vemuri, Y. Chen, and Z. Wang, "Registration assisted image smoothing and segmentation," *ECCV*, pp. 546–559, 2002.

[79] L. Vese and T. Chan, "A multiphase level set framework for image segmentation using the Mumford-Shah model," *Int. J.Comput. Vision*, vol. 50, pp. 271–293, 2002.

[80] P. Viola and W. Wells, "Alignement by maximization of mutual information," *IJCV*, 24, 2, pp. 137–154, 1997.

[81] F. Wang and B. Vemuri, "Simultaneous registration & segmentation of anatomical structures from brain MRI," *Proc.8th. Ann. Int. Conf. on Med. Image Comp. Computer-Assi. Interv. MICCAI*, pp. 17–25, 2005.

[82] M. Wang and S. Zhou, "Phase Field: A Variational Method for Structural Topology Optimization," *Computer Modeling in Engineering & Sciences*, vol. 6, no.6, pp. 547–566, 2004.

[83] W. Wells, P. Viola, H. Atsumi, S. Nakajima, and R. Kikinis, "Multi-Modal volume registration by maximization of mutual information," *Med. Image Anal.*, 1, 1, pp. 35–51, 1996.

[84] Wyatt, P. and Noble, J. "MRF-MAP joint segmentation and registration," *MICCAI*, pp. 580–587, 2002.

[85] J. Yang and J. Duncan, "3D image segmentation of deformable objects with shape apprearance joint prior models.," *MICCAI*, pp. 573–580, 2003.

[86] A. Yezzi, S. Kichenassamy, A. Kumar, P. Olver, and A. Tannenbaum, "A geometric snake model for segmentation of medical imagery," *IEEE Trans. Med. Imaging*, 16, pp. 199–209, 1997.

[87] A. Yezzi, A. Tsai, and A. Willsky, "A statistical approach to image segmentation for bimodal and trimodal imagery" *Proceedings of ICCV*, 1999.

[88] A. Yezzi, L. Zollei, and T. Kapur, "A variaional approach to joint segmentation and registration," *Proceedings of IEEE Conf. on Comp. Vis. Pat. Recog.*, 2001.

[89] A. Yezzi, L. Zollei, and T. Kapur, "A variaional approach to joint segmentation and registration through active contours," *Med. Image Anal.*, 7, pp. 171–185, 2003.

[90] Y. Young and D. Levy, "Registration-base morphing of active contours for segmentation of CT scans," *Math. Biosci. Eng.*, vol. 2, pp. 79–96, 2005.

[91] H. Zhao, T. Chan, B. Merriman, S. and Osher, "A variational level set approach to multiphase motion," *J. Comp. Phys.*, vol. 127, pp. 179–195, 1996.

[92] B. Zitova and J. Flusser, "Image registration methods: a survey," *Image Vis. Comp.*, 21. pp. 977–1000, 2003.

[93] S. Zhu and A. Yuille, "Region competition: unifying snakes, region growing, and Bayes/MDL for multiband image segmentation," *IEEE PAMI*, vol. 18, pp. 884–900, 1996.

BIOGRAPHICAL SKETCH

Jung-ha An was born in Chonju-si, Chollabuk-do, South Korea. She received her B.S. degree and M.S. degree from Chon-buk National University in 1995 and 1997 each. She joined the University of Florida in 1999 and received her Ph.D. in mathematics in 2005.

I certify that I have read this study and that in my opinion it conforms to acceptable standards of scholarly presentation and is fully adequate, in scope and quality, as a dissertation for the degree of Doctor of Philosophy.

Yunmei Chen, Chair
Professor of Mathematics

I certify that I have read this study and that in my opinion it conforms to acceptable standards of scholarly presentation and is fully adequate, in scope and quality, as a dissertation for the degree of Doctor of Philosophy.

David Groisser, Cochair
Associate Professor of Mathematics

I certify that I have read this study and that in my opinion it conforms to acceptable standards of scholarly presentation and is fully adequate, in scope and quality, as a dissertation for the degree of Doctor of Philosophy.

Jayadeep Gopalakrishnan
Special Member

I certify that I have read this study and that in my opinion it conforms to acceptable standards of scholarly presentation and is fully adequate, in scope and quality, as a dissertation for the degree of Doctor of Philosophy.

Shari Moskow
Associate Professor of Mathematics

I certify that I have read this study and that in my opinion it conforms to acceptable standards of scholarly presentation and is fully adequate, in scope and quality, as a dissertation for the degree of Doctor of Philosophy.

Murali Rao
Professor of Mathematics

I certify that I have read this study and that in my opinion it conforms to acceptable standards of scholarly presentation and is fully adequate, in scope and quality, as a dissertation for the degree of Doctor of Philosophy.

David Wilson
Professor of Mathematics

I certify that I have read this study and that in my opinion it conforms to acceptable standards of scholarly presentation and is fully adequate, in scope and quality, as a dissertation for the degree of Doctor of Philosophy.

Thomas Mareci
Associate Professor of Biochemistry and Molecular Biology

This dissertation was submitted to the Graduate Faculty of the Department of Mathematics in the College of Liberal Arts and Sciences and to the Graduate School and was accepted as partial fulfillment of the requirements for the degree of Doctor of Philosophy.

December 2005

_____

Dean, Graduate School

Various Methods in Shape Analysis and Image Segmentation and Registration

Jung-Ha An
(352) 392-0281
Department of Mathematics
Chair: Yunmei Chen
Degree: Doctor of Philosophy
Graduation Date: December 2005

The discovery of X-rays by German physicist Rontgen in 1895 initiated the history of medical imaging. Since then, many medical devices have been developed to diagnose and treat different diseases or to aid doctors during surgery. Image qualities which are produced by medical devices are not good enough to be applied to clinical research, therefore the development of mathematical algorithms has become necessary. The purpose of this dissertation is to discover the mathematical algorithms needed to improve these imaging problems, especially with an application to human heart and brain images. Suggested models in this dissertation with applications to medical imaging data show some promising results. In addition, these algorithms can be applied not only to medical imaging but also to general imaging.